

**Resonant Scattering of the He I 1.0833  $\mu$ m Triplet in H II Regions: Emission Spectra**B. T. DRAINE<sup>1</sup><sup>1</sup>*Dept. of Astrophysical Sciences, Princeton University, Princeton, NJ 08544, USA***ABSTRACT**

Resonant scattering of He I 1.0833  $\mu$ m triplet photons by metastable He 2  $^3S_1$  is studied for optical depths characteristic of H II regions. Regions with large He 2  $^3S_1$  column densities are predicted to have unusually broad multipeaked 1.0833  $\mu$ m emission profiles, with the centroid blue-shifted by up to  $\sim$ 14 km s $^{-1}$  relative to other lines. The feature FWHM can exceed 100 km s $^{-1}$  for some regions. Resonant trapping enhances dust absorption and reduces the He I 1.0833  $\mu$ m emission. Care must be taken when using the He I 1.0833  $\mu$ m/H I 1.0941  $\mu$ m (Pa $\gamma$ ) ratio to estimate the He $^+$ /H $^+$  ratio. Predicted spectra are computed for examples, including M17-B and NGC3603 in the Galaxy, and a star-forming region in M51. Observations of the 1.0833  $\mu$ m triplet with spectrometers such as NIRSPEC, CARMENES, or X-Shooter can confirm the predicted effects of resonant scattering in H II regions, and constrain the nebular conditions.

*Keywords:* galaxies: ISM

**1. INTRODUCTION**

The He I 1.0833  $\mu$ m triplet is typically the strongest observable emission line generated when He $^+$  recombines with electrons. It has been observed in emission from H II regions powered by O stars (L. H. Aller & W. Liller 1959), from planetary nebulae (W. Liller & L. H. Aller 1963; C. R. O'Dell 1963), from AGNs (P. D. Levan et al. 1981) and QSOs (P. D. Levan et al. 1984), and from the Earth's thermosphere (e.g., S. R. Kulkarni 2025).

Emission of 1.0833  $\mu$ m triplet photons populates the metastable He $^0$  1s2s 2  $^3S_1$  level, and the 2  $^3S_1$  level population can become large enough to produce observable absorption. W. S. Adams (1949) detected interstellar He $^0$  2  $^3S_1$  – 4  $^3P^o$  3890  $\text{\AA}$  absorption toward O stars in the Orion Nebula and the Trifid Nebula, and absorption in the He $^0$  2  $^3S_1$  – 2  $^3P^o_1$  1.0833  $\mu$ m triplet itself was observed by G. A. Galazutdinov & J. Krelowski (2012) toward the O9.5V star  $\zeta$  Oph. In all of these detections, the metastable He $^0$  2  $^3S_1$  resides in the H II region around a hot star. N. Indriolo et al. (2009) searched for but failed to detect He I 1.0833  $\mu$ m absorption in the diffuse neutral ISM outside of H II regions, placing an upper limit on the cosmic ray ionization rate.

The 1.0833  $\mu$ m triplet is also observed in absorption in some QSOs (K. M. Leighly et al. 2011; X. Pan et al. 2019), in the Solar chromosphere (e.g., A. G. M. Pietrow et al. 2025), and in transiting exoplanets with extended atmospheres (M. Mansfield et al. 2018; L. Nortmann et al. 2018; A. Oklopčić & C. M. Hirata 2018; R. Allart et al. 2019). Spectra of the extragalactic “Little Red Dots” also show evidence of 1.0833  $\mu$ m absorption (e.g., B. Wang et al. 2025).

S. R. Pottasch (1962) and R. R. Robbins (1968a,b) discussed the effects on the populations of other He I levels in H II regions and planetary nebulae when transitions to 2  $^3S_1$  become optically thick. Absorption by the metastable 2  $^3S_1$  level can suppress emission in some lines (e.g., He I 3890  $\text{\AA}$ , 3188  $\text{\AA}$ ) and enhance emission in certain other lines (e.g., He I 7067  $\text{\AA}$ , 4713  $\text{\AA}$ ) (R. R. Robbins 1968b; R. A. Benjamin et al. 2002; K. P. M. Blagrave et al. 2007). The theory was applied to interpret He I line emission from the Orion Nebula (K. P. M. Blagrave et al. 2007; R. L. Porter et al. 2007).

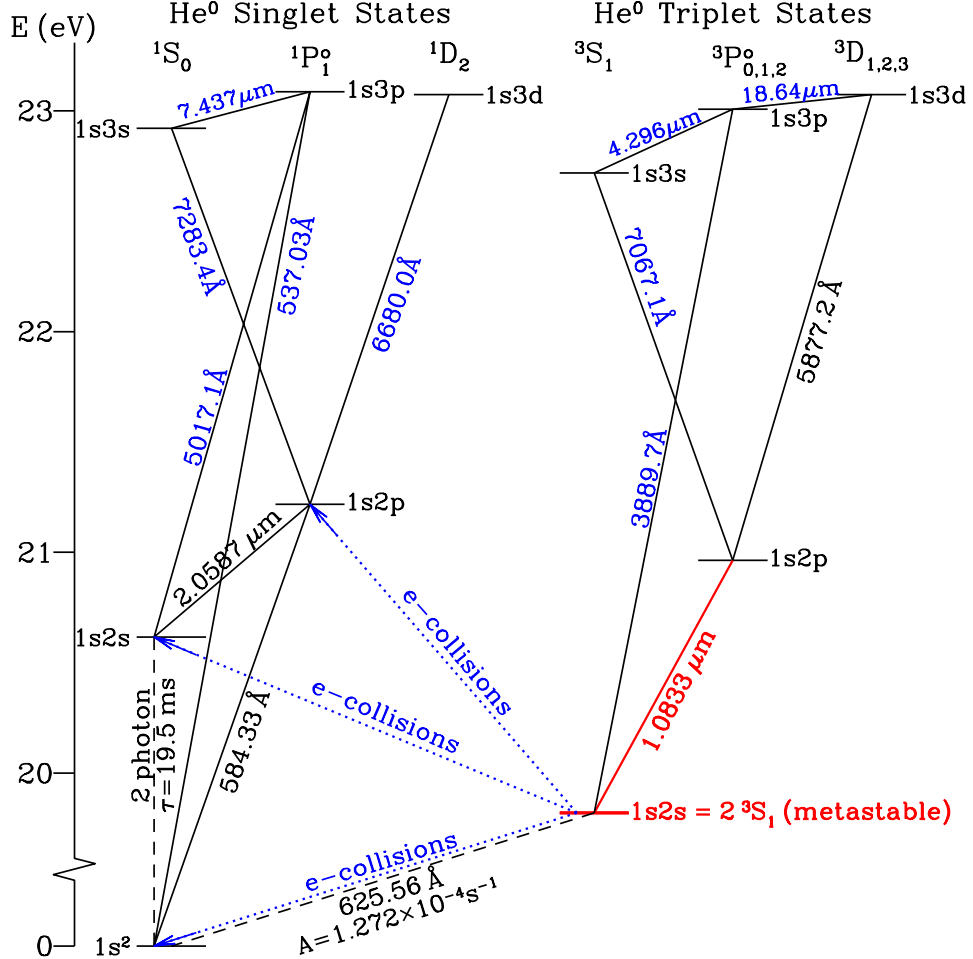


**Figure 1.** Energy levels of He I below 23.5 eV. Permitted transitions are shown as solid lines, with the  $1.0833\mu\text{m}$  triplet shown in red. Dashed lines indicate forbidden transitions. Dotted lines show the principal paths for collisional depopulation of  $2^3\text{S}_1$  by electrons.

Previous studies were concerned with the important effects of resonant scattering on the overall strengths of He I emission lines. The present paper is concerned with the *spectrum* of the He I  $1.0833\mu\text{m}$  triplet when observed in emission. For realistic conditions, the spectrum of the  $1.0833\mu\text{m}$  photons escaping from the H II region can be substantially altered by resonant scattering. As a result, the  $1.0833\mu\text{m}$  triplet is predicted to have unusual multi-peaked emission profiles. The emission spectrum is sensitive to the column density of metastable  $\text{He}^0 2^3\text{S}_1$ , and to the velocity dispersion of the recombining  $\text{He}^+$  that is responsible for populating the  $2^3\text{S}_1$  level. Therefore, observational determination of the actual line profile will provide a new diagnostic for the nebular conditions. It also will serve as a test for our theoretical understanding of resonant scattering.

The relevant atomic physics is reviewed in Section 2. Section 3 outlines the radiative transfer problem. Section 4 presents the results of Monte-Carlo simulations for dustless H II regions, while Section 5 includes the effects of dust absorption. The results are discussed in Section 6 and summarized in Section 7. Details of the Monte Carlo procedures are provided in the Appendix.

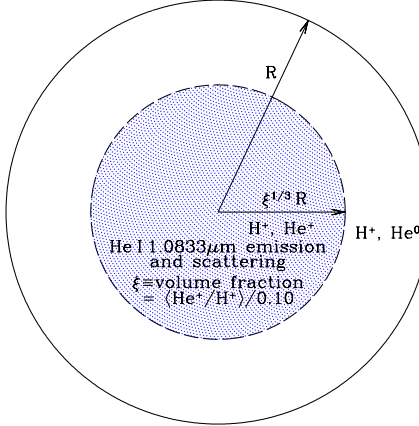


**Figure 2.** H II region cross-section.  $\xi$  is the fraction of the volume where He is mainly  $\text{He}^+$ .

## 2. THE METASTABLE $2^3\text{S}_1$ LEVEL

### 2.1. Population by Recombination

Figure 1 shows the first 11 energy levels of He I. Approximately 3/4 of the radiative recombinations of  $\text{He}^+$  with electrons populate the triplet states of He I, and essentially 100% of the triplet recombinations end up populating the lowest energy triplet state,  $2^3\text{S}_1$ .

The  $1s2s\ 2^3\text{S}_1$  level is metastable, with a probability per unit time  $A_{\text{ms}} = 1.272 \times 10^{-4} \text{ s}^{-1}$  (W. L. Wiese & J. R. Fuhr 2009) for decay to the  $1s^2\ 1\text{S}_0$  ground state with emission of a  $625.56\text{ \AA}$  photon. The density of  $\text{He}^0\ 2^3\text{S}_1$  is

$$n(2^3\text{S}_1) = \frac{\alpha_{\text{trip}} n_e n(\text{He}^+)}{A_{\text{ms}} + n_e k_d} \quad , \quad (1)$$

where  $n_e$  is the electron density,  $\alpha_{\text{trip}}$  is the rate coefficient for radiative recombination of  $\text{He}^+$  to the triplet states of  $\text{He}^0$ , and  $k_d$  is the rate coefficient for collisional depopulation of  $2^3\text{S}_1$  by transitions to singlet states.<sup>2</sup>

A uniform density Strömgren sphere with H photoionization rate<sup>3</sup>  $Q_0 = 10^{48} Q_{48} \text{ s}^{-1}$  and  $n_e = 10^3 n_3 \text{ cm}^{-3}$  has H fully ionized out to radius

$$R = 9.88 \times 10^{17} Q_{48}^{1/3} n_3^{-2/3} \text{ cm} \quad , \quad (2)$$

and center-to-edge emission measure

$$\text{EM}_R \equiv \int_0^R n_e n(\text{H}^+) dr = 9.88 \times 10^{23} Q_{48}^{1/3} n_3^{4/3} \text{ cm}^{-5} \quad . \quad (3)$$

Let  $\xi$  be the fraction of the volume within which He is singly-ionized (see Figure 2). For helium abundance  $n_{\text{He}}/n_{\text{H}} = 0.10$  (as will be assumed here),  $\xi \approx \min(6.5Q_1/Q_0, 1)$ , where  $Q_1$  is the stellar output of  $h\nu > 24.6\text{ eV}$  photons (see, e.g., B. T. Draine 2011a). The center-to-edge column density of metastable  $\text{He}^0\ 2^3\text{S}_1$

$$N_R(2^3\text{S}_1) \equiv \int_0^R n(2^3\text{S}_1) dr \approx 1.71 \times 10^{14} \text{ cm}^{-2} \xi^{1/3} \frac{Q_{48}^{1/3} n_3^{4/3}}{(1 + 0.26n_3)} \quad (4)$$

<sup>2</sup> For  $T_e = 9 \times 10^3 \text{ K}$ ,  $\alpha_{\text{trip}} \approx 2.42 \times 10^{-13} \text{ cm}^3 \text{ s}^{-1}$  (G. Del Zanna & P. J. Storey 2022), and  $k_d \approx 3.3 \times 10^{-8} \text{ cm}^3 \text{ s}^{-1}$  (I. Bray et al. 2000). He I  $2^3\text{S}_1$  can also be depopulated by photoionization by  $h\nu > 4.77\text{ eV}$  photons, including Lyman- $\alpha$  (D. E. Osterbrock 1989), but this is usually subdominant.

<sup>3</sup> When dust is present,  $Q_{48}$  should be understood to be the actual H photoionization rate, not the stellar output of H-ionizing photons.

**Table 1.** He I  $1.0833\mu\text{m}$  Triplet<sup>a</sup>

$\ell$	$u$	$J_u$	$g_u$	$A_{u\ell} (\text{s}^{-1})$	$\lambda (\mu\text{m})$	$\lambda_{\text{air}} (\mu\text{m})$	$v_u (\text{km s}^{-1})^b$
$2^3\text{S}_1$	$2^3\text{P}_0^o$	0	3	$1.0216 \times 10^7$	1.083205748	1.082909115	-29.96
$2^3\text{S}_1$	$2^3\text{P}_1^o$	1	9	$1.0216 \times 10^7$	1.083321676	1.083025011	+2.19
$2^3\text{S}_1$	$2^3\text{P}_2^o$	2	15	$1.0216 \times 10^7$	1.083330645	1.083033978	+4.67
$2^3\text{S}_1$	$2^3\text{P}^o$	1,2,3	27	$1.0216 \times 10^7$	1.083313778	1.083017115	0

<sup>a</sup> NIST Atomic Physics Database ([A. E. Kramida et al. 2024](#))

<sup>b</sup> Doppler shift relative to centroid.

can exceed  $10^{14} \text{ cm}^{-2}$ .

## 2.2. Radiative Transfer

Most of the radiative recombinations to the He<sup>0</sup> triplet states pass through  $2^3\text{P}_{0,1,2}^o$ , resulting in emission of a photon in the  $1.0833\mu\text{m}$  triplet (see Table 1). The  $2^3\text{P}_j^o$  created either by direct recombination or by radiative decay from higher levels will have a Maxwellian velocity distribution, and newly-injected  $2^3\text{P}_j^o \rightarrow 2^3\text{S}_1$  photons emitted by these atoms will be created with a Voigt line profile,<sup>4</sup> characterized by the usual Doppler broadening parameter  $b$  and a “damping constant”

$$a_{u\ell} \equiv \frac{\gamma_{u\ell} \lambda_{u\ell}}{4\pi b} \quad , \quad (5)$$

where  $\gamma_{u\ell}$  is the sum of the transition probabilities for depopulating levels  $u$  and  $\ell$ . Thermal broadening alone gives

$$b_{\text{therm}} = \left( \frac{2kT}{m_{\text{He}}} \right)^{1/2} = 6.45 \left( \frac{T}{10^4 \text{ K}} \right)^{1/2} \text{ km s}^{-1} \quad ; \quad (6)$$

turbulence in the H II region will result in  $b > b_{\text{therm}}$ . For H II regions, we consider four cases:  $b = 6.45, 10, 15$ , and  $20 \text{ km s}^{-1}$ . The He I  $1.0833\mu\text{m}$  triplet lines each have

$$a_{u\ell} \equiv \frac{A_{u\ell} \lambda_{u\ell}}{4\pi b} = 8.807 \times 10^{-5} \left( \frac{10 \text{ km s}^{-1}}{b} \right) \quad , \quad (7)$$

since the lifetime of  $2^3\text{S}_1$  is long compared to the  $10^{-7} \text{ s}$  lifetime of  $2^3\text{P}_J^o$ .

Newly-emitted  $1.0833\mu\text{m}$  triplet photons may be absorbed by another He atom in the metastable  $2^3\text{S}_1$  level. The center-to-edge line-center optical depth for  $2^3\text{S}_1 \rightarrow 2^3\text{P}_J^o$  absorption is

$$\tau_0(2^3\text{S}_1 \rightarrow 2^3\text{P}_J^o) = (2J+1) \frac{A_{u\ell} \lambda_{u\ell}^3}{8\pi^{3/2}} \left( \frac{N_R(2^3\text{S}_1)}{b} \right) \quad (8)$$

$$= 29.2(2J+1) \left( \frac{N_R(2^3\text{S}_1)}{10^{14} \text{ cm}^{-2}} \right) \left( \frac{10 \text{ km s}^{-1}}{b} \right) \quad . \quad (9)$$

## 2.3. The $1.0833\mu\text{m}$ Multiplet

The three He I  $2^3\text{S}_1 - 2^3\text{P}_J^o$  lines have line shifts

$$v_{u\ell} \equiv c \left[ 1 - \frac{\lambda_c}{\lambda_{u\ell}} \right] \quad (10)$$

<sup>4</sup> Many authors approximate the spectrum of the newly-injected photons as a simple Gaussian profile corresponding to the thermal velocity distribution, but for large  $\tau_0$  the small fraction of photons injected in the “damping wings”, with much higher escape probabilities, should not be neglected.

of  $-29.96$ ,  $+2.19$ , and  $+4.67$  km s $^{-1}$  relative to the centroid wavelength  $\lambda_c = 1.0833138\mu\text{m}$  (see Table 1). Because the splittings are small, the multiplet is often treated as a single line (e.g., R. R. Robbins 1968b; R. A. Benjamin et al. 2002). Here we treat each line separately.

Scattering by a multiplet is identical to scattering by a single line, except that one must allow for the possibility of the photon being scattered by any one of the transitions in the multiplet. For a uniform sphere, the He I 1.0833 $\mu$ m scattering problem is characterized by two parameters: (1) the Doppler broadening parameter  $b$ , and (2) the sum of the line-center optical depths of the three contributing line profiles,

$$\tau_{\text{tot}} \equiv \sum_{J=0}^2 \tau_0(2^3\text{S}_1 \rightarrow 2^3\text{P}_J^o) = 262 \left( \frac{N_R(2^3\text{S}_1)}{10^{14} \text{ cm}^{-2}} \right) \left( \frac{10 \text{ km s}^{-1}}{b} \right) \quad (11)$$

$$\approx 448 \frac{\xi^{1/3} Q_{48}^{1/3} n_3^{4/3}}{(1 + 0.26n_3)} \left( \frac{10 \text{ km s}^{-1}}{b} \right) . \quad (12)$$

### 3. RESONANT SCATTERING

Resonant scattering for a single line was discussed by W. Unno (1952), G. B. Field (1959), D. G. Hummer (1962), and many subsequent papers, with particular attention to the scattering of the H Lyman  $\alpha$  line (e.g., J. R. M. Bonilha et al. 1979; D. A. Neufeld 1990; Z. Zheng & J. Miralda-Escudé 2002; M. Dijkstra 2019; K.-i. Seon & C.-G. Kim 2020). Here we consider resonant scattering of He I 1.0833 $\mu$ m triplet photons.

We assume a spherical H II region with uniform electron density  $n_e$  and He $^+$  density  $n(\text{He}^+)$ . The recombining He $^+$  results in a uniform density of metastable He I 2 $^3\text{S}_1$ . 1.0833 $\mu$ m triplet photons are randomly injected with initial frequency drawn from the Voigt profile for emission from 2 $^3\text{P}_J^o$  with the Maxwellian velocity distribution of the recombining He $^+$ . Once emitted, the photons travel until they either scatter or escape the H II region. The scattering is treated using the full 3-line multiplet, with a Voigt absorption profile for each line.

If scattering takes place, the scattered photon travels in a new direction with a new frequency. The new direction is drawn from the scattering phase function for electric dipole scattering. The new frequency is drawn from the “partial redistribution function”  $R_{\text{II-B}}$  (D. G. Hummer 1962) that describes coherent scattering by a Maxwellian distribution of atoms with finite natural linewidth.<sup>5</sup> The present radiative transfer treatment neglects Thomson scattering by electrons, but allows for absorption by dust. Our Monte-Carlo methodology for scattering in a multiplet is described in the Appendix. Complete numerical results can be obtained from <https://doi.org/10.7910/DVN/EOHGDD>.

## 4. HE I 1.0833 $\mu$ m EMISSION FROM DUSTLESS H II REGIONS

### 4.1. Number of Scatterings and Escape Probability

Let  $\tau_0$  be the line-center optical depth from center to edge of a spherical H II region. If no dust is present, there are no processes leading to photon loss, hence every injected triplet photon eventually escapes. Let  $\langle N_{\text{sca}} \rangle$  be the mean number of scatterings per injected photon. We define the “escape probability” to be

$$\beta \equiv \frac{1}{1 + \langle N_{\text{sca}} \rangle} , \quad (13)$$

i.e., the fraction of the escape attempts that succeed.

For scattering by a single resonant line (e.g., Lyman  $\alpha$ , or He I 1.0833 $\mu$ m approximated as a single line),  $\langle N_{\text{sca}} \rangle$  is shown as a function of  $\tau_0$  in Figure 3a, for two values of the damping constant

<sup>5</sup> The frequency redistribution function is sampled using the “rejection method” (W. H. Press et al. 1992; Z. Zheng & J. Miralda-Escudé 2002).

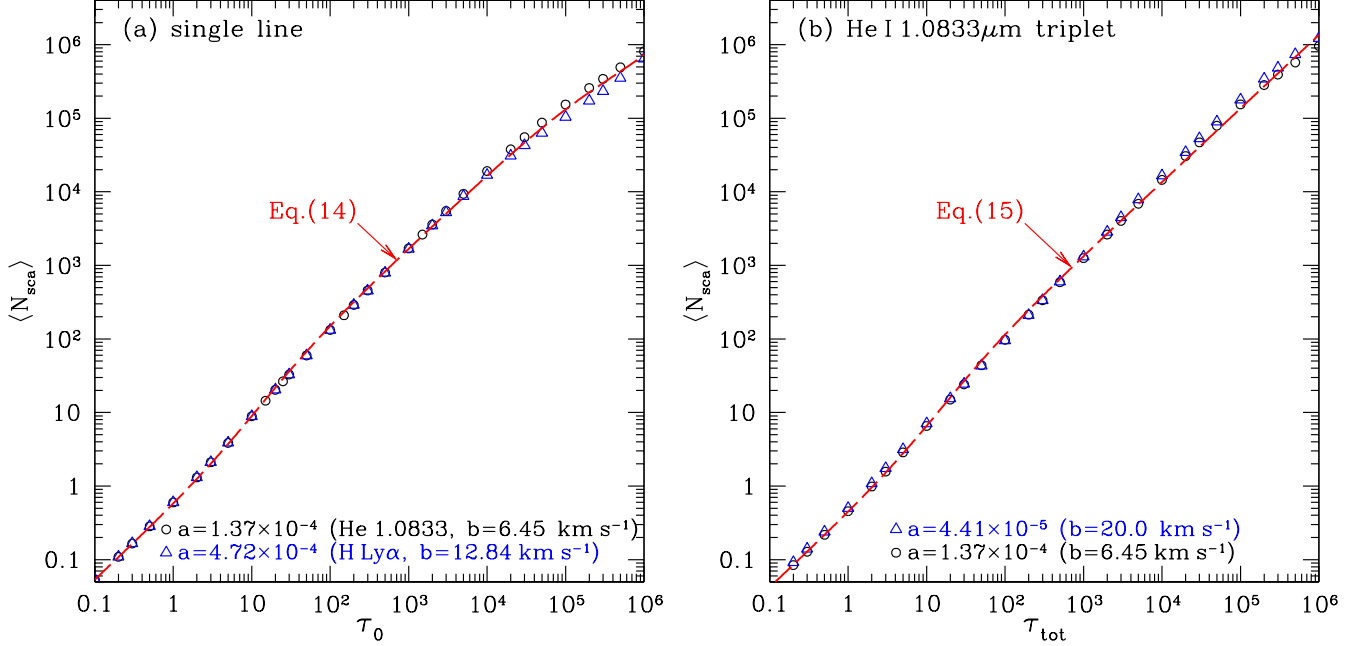


**Figure 3.** Number of scatterings for spherical geometry for (a) single resonance line (e.g., Lyman  $\alpha$ ), for two values of the damping constant  $a$ . (b) He I  $1.0833\mu\text{m}$  triplet, for two values of  $b$ . The approximations (14) and (15) are shown as dashed red curves.

a. For given  $\tau_0$ ,  $\langle N_{\text{sca}} \rangle$  is almost independent of  $a$  – note the small difference between  $\langle N_{\text{sca}} \rangle$  for  $a = 1.37 \times 10^{-4}$  and  $4.72 \times 10^{-4}$ .

For scattering by a single line (e.g., Lyman  $\alpha$ ),  $\langle N_{\text{sca}} \rangle$  can be approximated by the fitting function

$$N_{\text{sca},1} \approx \frac{3}{\sqrt{8}} \tau_0 \left[ 1 + \frac{0.1 \tau_0}{(1 + 0.045 \tau_0)(1 + 5 \times 10^{-6} \tau_0)} \right] , \quad (14)$$

shown in Figure 3a. Equation (14) is exact in the limit  $\tau_0 \rightarrow 0$ , and provides a good approximation for single-line scattering for  $\tau_0 \lesssim 10^6$ .

Figure 3b shows  $\langle N_{\text{sca}} \rangle$  calculated for the He I  $1.0833\mu\text{m}$  triplet, for two values of  $b$ . As for the single-line case in Figure 3a,  $\langle N_{\text{sca}} \rangle$  is almost independent of  $b$ . While  $\langle N_{\text{sca}} \rangle$  is similar to the single-line result, it differs in detail. For the He I triplet,  $\langle N_{\text{sca}} \rangle$  can be approximated by

$$N_{\text{sca},3} \approx 0.42 \tau_{\text{tot}} \frac{(1 + 0.11 \tau_{\text{tot}})}{(1 + 0.034 \tau_{\text{tot}})} , \quad (15)$$

shown in Figure 3b. Equation (15) provides a good approximation for  $\langle N_{\text{sca}} \rangle$  for the He I  $1.0833\mu\text{m}$  triplet for  $\tau_{\text{tot}} \lesssim 10^6$ , for a range of  $b$  values.

The escape probability  $\beta$  defined by Equation (13) is shown for single-line scattering in Figure 4a. R. A. Benjamin et al. (2002, hereafter BSS02) approximated the triplet as a single line, and estimated the escape probability by integrating the “escape function”  $\epsilon(\tau_\nu)$  (D. P. Cox & W. G. Mathews 1969) over a Maxwellian line profile. This integral, labelled  $\beta_{\text{BSS02}}$ , is shown in Figure 4. For scattering of a single line in a spherical nebula,  $\beta_{\text{BSS02}}$  overestimates  $\beta$  for  $\tau_{\text{tot}} \gtrsim 10$ , exceeding  $\beta$  by a factor  $\sim 5$  at  $\tau_{\text{tot}} = 10^4$ .

It is not surprising that our calculation of  $\beta$  differs from  $\beta_{\text{BSS02}}$ : they are different quantities. Our definition of  $\beta$  (see Equation 13) is based on the mean number of scatterings per injected photon,

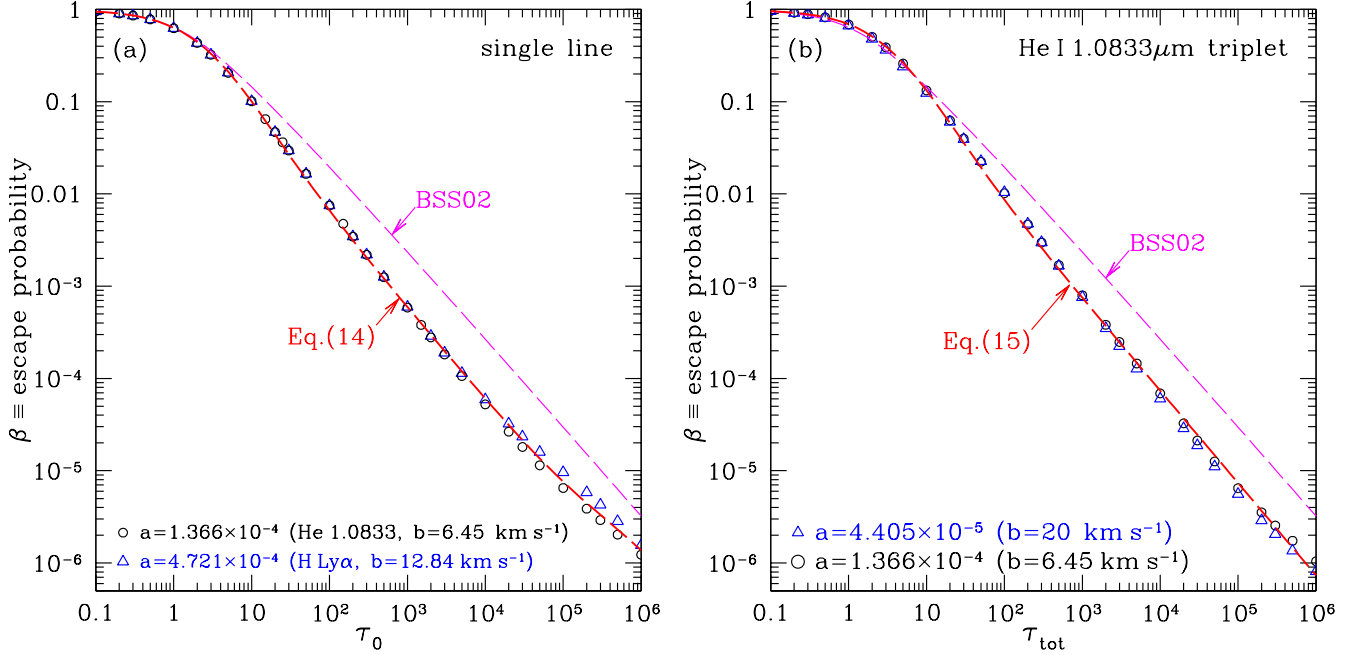


**Figure 4.** Escape probability  $\beta \equiv 1/(1 + \langle N_s \rangle)$  as a function of optical depth. (a) Single resonant line, for spherical geometry, and  $a = 1.37 \times 10^{-4}$  (appropriate for He I  $1.0833\mu\text{m}$ ) and  $a = 4.72 \times 10^{-4}$  (appropriate for H I Ly $\alpha$ ). Also shown:  $\beta$  calculated using Eq. (14), and the escape probability  $\beta_{\text{BSS02}}$  estimated by R. A. Benjamin et al. (2002). (b) Full three-line treatment for the He I  $1.0833\mu\text{m}$  triplet for spherical geometry, for two values of  $b$ . Also shown:  $\beta$  calculated using Eq. (15), and  $\beta_{\text{BSS02}}$ .

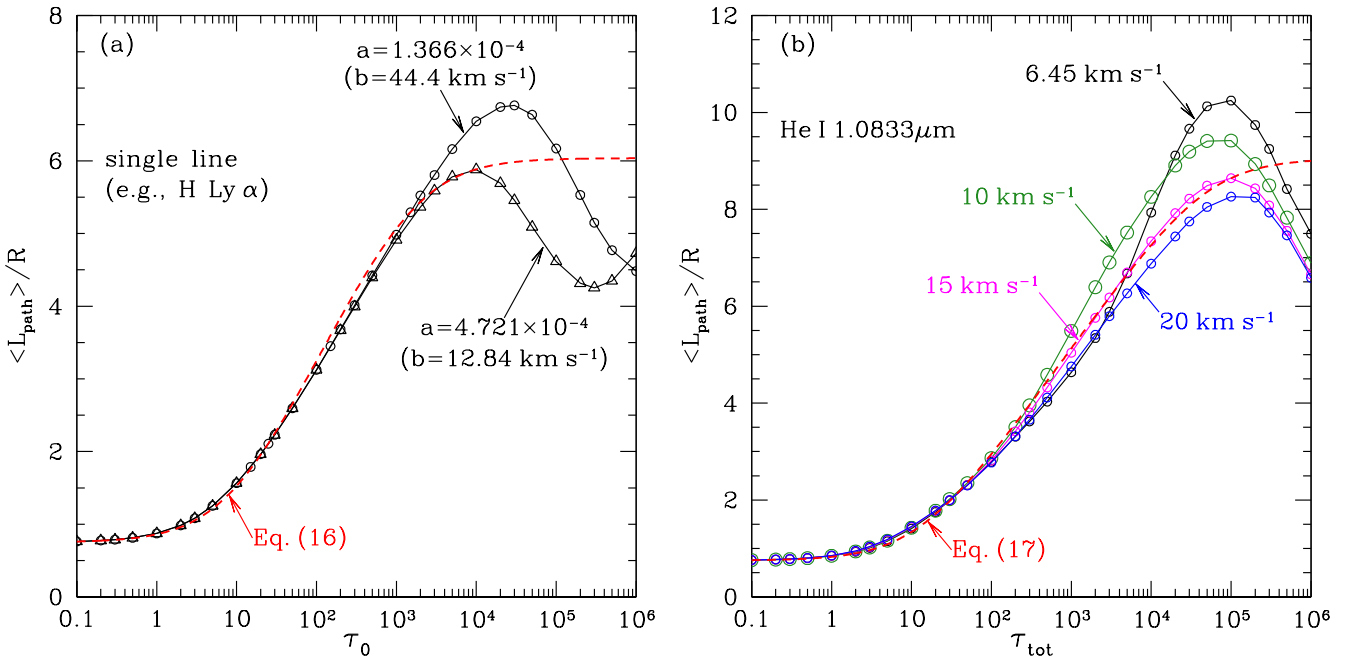


**Figure 5.**  $\langle L_{\text{path}} \rangle / R$ , where  $\langle L_{\text{path}} \rangle$  is average path length traveled by photons before escaping from a sphere of radius  $R$ . (a) Results for a single line (e.g., Ly $\alpha$ ) for two values of  $a$ . The dashed line is an empirical fit (Eq. 16). (b) Results for the He I  $1.0833\mu\text{m}$  triplet for 4 values of  $b$ . The dashed line is an empirical fit (Eq. 17).

allowing the spectrum to be modified by the scattering process, whereas  $\beta_{\text{BSS02}}$  is defined to be the probability of escape *without* scattering for photons with a Maxwellian line profile.

Figure 4b shows  $\beta$  calculated for the He I 1.0833 $\mu\text{m}$  triplet, for  $b = 6.45$  and 20 km s $^{-1}$ . For a single line,  $\beta(\tau_0)$  is independent of  $b$ , except for a weak dependence via the damping constant  $a$ . For the full 3-line treatment for the He I 1.0833 $\mu\text{m}$  triplet,  $\beta(\tau_{\text{tot}})$  depends only weakly on  $b$ . Comparing Figures 4a and 4b, we see that  $\beta$  calculated using the full three-line treatment for He I 1.0833 $\mu\text{m}$  is similar to – but slightly below – the results of the single-line approximation. For  $6 \lesssim b \lesssim 20$  km s $^{-1}$ , the fitting function (15) provides a good approximation for scattering of He I triplet photons (see Figure 4b).

#### 4.2. Path Length

Scattering affects the path length traversed by photons before escaping the scattering volume. Figure 5 shows the mean distance  $\langle L_{\text{path}} \rangle$  traveled by photons before leaving the sphere. As  $\tau_{\text{tot}}$  increases,  $L_{\text{path}}/R$  increases slowly, peaking near  $\tau_{\text{tot}} \approx 10^5$ . Figure 5a shows results for scattering by a single line (e.g., Ly  $\alpha$ ), for two different values of  $a$ . For  $\tau \lesssim 10^4$ ,  $\langle L_{\text{path}} \rangle$  is approximated by

$$\frac{\langle L_{\text{path}} \rangle}{R} \approx \ln \left[ e^{3/4} + \frac{0.25\tau_0}{(1 + 0.0006\tau_0)} \right] \quad \text{for a single line} \quad . \quad (16)$$

The path length for He I 1.0833 $\mu\text{m}$  triplet photons is shown in Figure 5b for  $\tau_{\text{tot}} < 10^6$ . For  $\tau_{\text{tot}} \lesssim 10^{4.5}$ ,  $\langle L_{\text{path}} \rangle$  can be approximated by the fitting function

$$\frac{\langle L_{\text{path}} \rangle}{R} \approx \ln \left[ e^{3/4} + \frac{0.17\tau_{\text{tot}}}{(1 + 2 \times 10^{-5}\tau_{\text{tot}})} \right] \quad \text{for He I 1.0833}\mu\text{m} \quad . \quad (17)$$

The residence time within the H II region per injected photon is just  $L_{\text{path}}/c$ , hence the energy density of 1.0833 $\mu\text{m}$  triplet photons will be

$$\langle u_{1.0833} \rangle = \frac{\alpha_{\text{trip}} n_e n(\text{He}^+) R}{c} \left( \frac{\langle L_{\text{path}} \rangle}{R} \right) \left( \frac{hc}{\lambda} \right) \quad . \quad (18)$$

#### 4.3. Spectrum

For single-line scattering, the spectrum of the escaping photons is shown in Figure 6a for  $b = 6.45$  km s $^{-1}$  and five values of  $\tau_{\text{tot}}$ . Single-line scattering generates a symmetric line profile. For  $\tau_{\text{tot}} \lesssim 5$ , the profile is centrally-peaked, while for  $\tau_{\text{tot}} \gtrsim 10$  it develops a central minimum, with two symmetric peaks; as  $\tau_{\text{tot}}$  increases, the central minimum deepens, and the peaks are increasingly red-shifted and blue-shifted. Figure 6a shows the profiles for  $b = 6.45$  km s $^{-1}$ , but the problem is self-similar,<sup>6</sup> with the profile width (for fixed  $\tau_0$ ) proportional to  $b$ .

Figure 6b shows line profiles calculated for the same velocity dispersion as in Figure 6a, and the same values of  $\tau_{\text{tot}}$ , but for the full 1.0833 $\mu\text{m}$  triplet. The line profiles in Figure 6b are qualitatively different from Figure 6a.

The *shape* of the profile of escaping He I 1.0833 $\mu\text{m}$  photons depends on  $b$  as well as  $\tau_{\text{tot}}$ . Our discussion here follows the results for  $b = 6.45$  km s $^{-1}$  (Figure 6b). In the optically-thin limit  $\tau_{\text{tot}} \lesssim 1$ , the line profile resolves into two components; 8/9 of the power is in the blended emission at 1.08333 $\mu\text{m}$  from  $2^3\text{P}_1^o$  and  $2^3\text{P}_2^o$ , and 1/9 of the power is in the 1.08321 $\mu\text{m}$  line from  $2^3\text{P}_0^o$ . As  $\tau_{\text{tot}}$  increases, the line profile departs from the simple optically-thin profile, as shown in Figures 6b, 7a, and 7b. First, the blended emission from  $2^3\text{P}_1^o$  and  $2^3\text{P}_2^o$  broadens, and for  $\tau_{\text{tot}} \gtrsim 5$  develops a central minimum,

<sup>6</sup> Except for a weak dependence on  $a \propto b^{-1}$ .

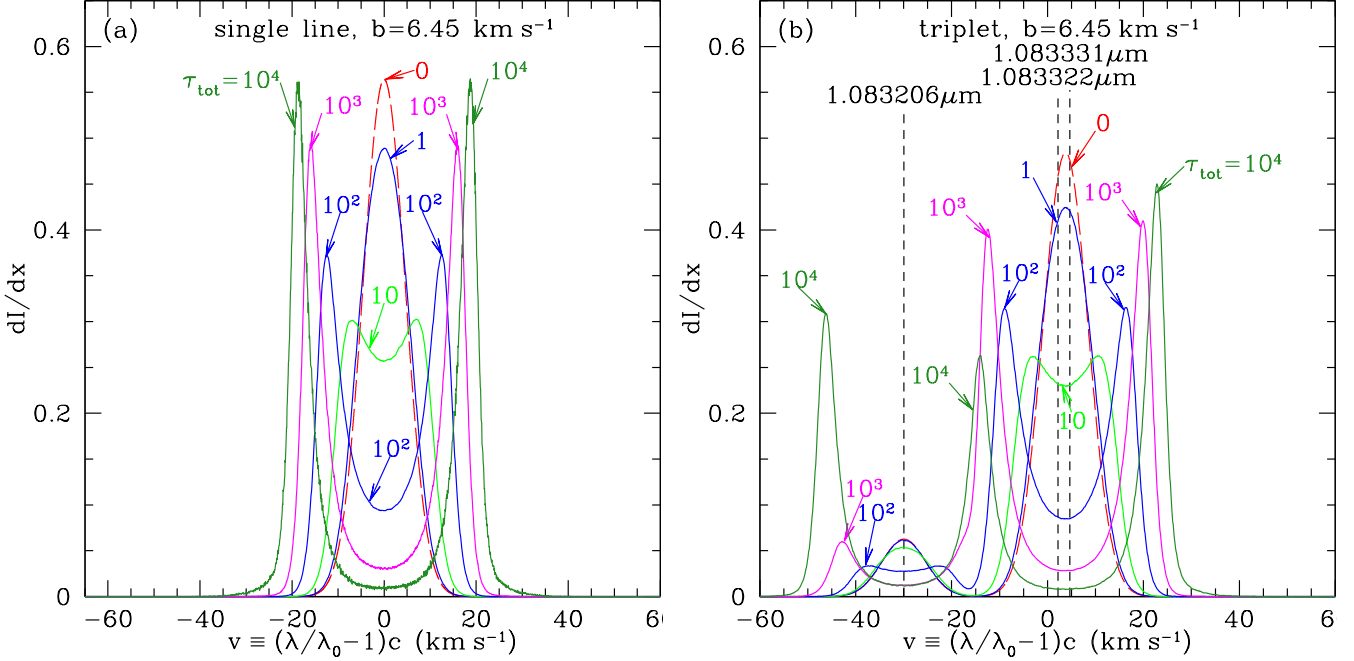


**Figure 6.** Spectra  $dI/dx$  of escaping photons for dustless H II regions with  $b = 6.45 \text{ km s}^{-1}$ , for various values of the line-center optical depth  $\tau_{\text{tot}}$ . The normalization is  $\int I dx = 1$ , where  $x \equiv (\lambda_0/\lambda - 1)(c/b)$ . Velocity  $v$  is relative to the centroid  $\lambda_0$  for optically-thin absorption. (a) Single-line scattering (e.g., Lyman  $\alpha$ ). (b) The He I  $1.0833\mu\text{m}$  triplet. Spectra are shown for  $\tau_{\text{tot}} = 0, 1, 10, 10^2, 10^3$ , and  $10^4$ ; profiles are labelled by  $\tau_{\text{tot}}$ . The single-line profiles (panel a) are symmetric, while the triplet profiles (panel b) are asymmetric. For the same  $b$  and  $\tau_{\text{tot}}$ , the triplet profile is blue-shifted and broader than would be predicted for a single-line treatment.

so that for  $\tau_{\text{tot}} = 10$  the line profile has three peaks: two of the peaks are approximately symmetric around the (blended)  $2^3\text{P}_1^o$  and  $2^3\text{P}_2^o$  lines, and the third is at the wavelength of the weaker emission at  $1.08321\mu\text{m}$  from  $2^3\text{P}_0^o$ . For  $\tau_{\text{tot}} \gtrsim 50$  the  $1.08321\mu\text{m}$  line also develops a central minimum. For  $\tau_{\text{tot}} \gtrsim 10^4$  the outer two peaks become increasingly dominant, moving farther apart in wavelength with increasing  $\tau_{\text{tot}}$ .

The one-line treatment generates a symmetric profile, with no overall redshift or blue shift. The three-line treatment, however, produces an overall blue shift of the emitted photons when  $\tau_{\text{tot}} \gtrsim 10$ , because some of the photons emitted by  $2^3\text{P}_{1,2}^o$  scatter blueward and are then subject to scattering in the  $2^3\text{S}_1 - 2^3\text{P}_0^o$  transition. The mean blueshift of the escaping photons is shown in Figure 8. For  $b \gtrsim 10 \text{ km s}^{-1}$  and  $100 \lesssim \tau_{\text{tot}} \lesssim 3 \times 10^4$ , Figure 8 shows that the He I  $1.0833\mu\text{m}$  triplet is predicted to have a mean blueshift exceeding  $10 \text{ km s}^{-1}$  relative to the other He I and H I recombination lines.

In addition to producing a systematic blue shift of the He I  $1.0833\mu\text{m}$  emission, resonant scattering broadens the line profile. Figure 9 shows the full-width-at-half-maximum (FWHM) of the emission profile. For small  $\tau_{\text{tot}}$  the FWHM has values appropriate to optically-thin emission: for small  $\tau_{\text{tot}}$  the FWHM is not affected by the weak line because it remains below 50% of the peak. As  $\tau_{\text{tot}}$  is increased, the FWHM increases discontinuously when the line profile develops a peak blueward of  $1.0832\mu\text{m}$  that rises to 50% of the peak intensity. For  $b \approx 10 \text{ km s}^{-1}$ , the FWHM can exceed  $75 \text{ km s}^{-1}$  for  $\tau_{\text{tot}} \gtrsim 10^2$ .

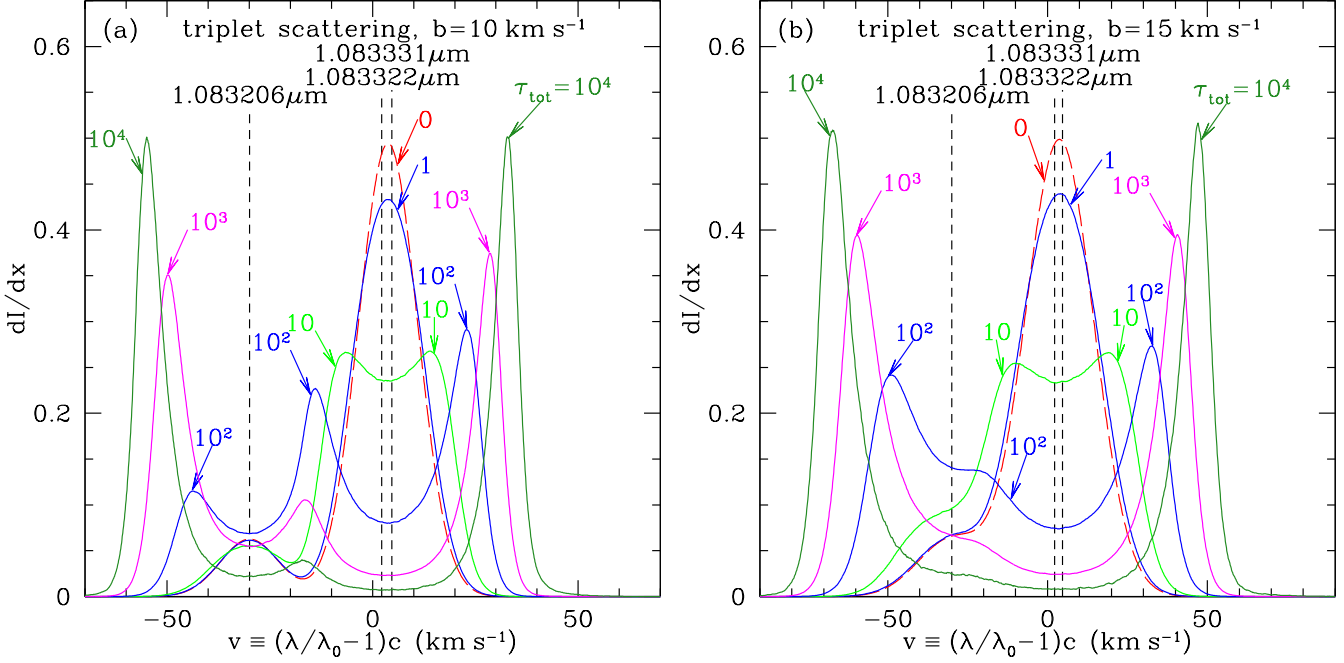


**Figure 7.** Same as Figure 6b, but for (a)  $b = 10 \text{ km s}^{-1}$ , and (b)  $b = 15 \text{ km s}^{-1}$ . For each case, results are shown for  $\tau_{\text{tot}} = 0, 1, 10, 10^2, 10^3$ , and  $10^4$ ; curves are labelled by  $\tau_{\text{tot}}$ . Note the increased splitting for  $b = 15 \text{ km s}^{-1}$  relative to  $b = 10 \text{ km s}^{-1}$  (panel a) or  $b = 6.45 \text{ km s}^{-1}$  (Figure 6b).

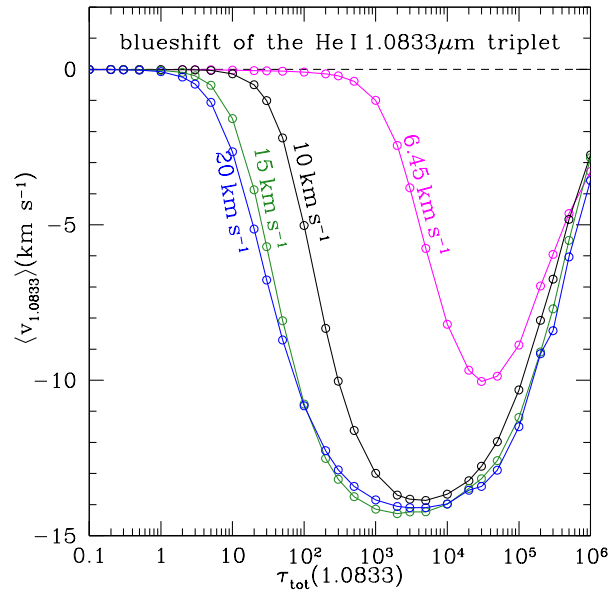


**Figure 8.** Overall blue shift of radiation from the He I  $1.0833 \mu\text{m}$  triplet, as a function of the optical depth  $\tau_{\text{tot}}$  of the He I  $1.0833 \mu\text{m}$  triplet, for He I velocity  $b = 6.45, 10, 15, 20 \text{ km s}^{-1}$ .

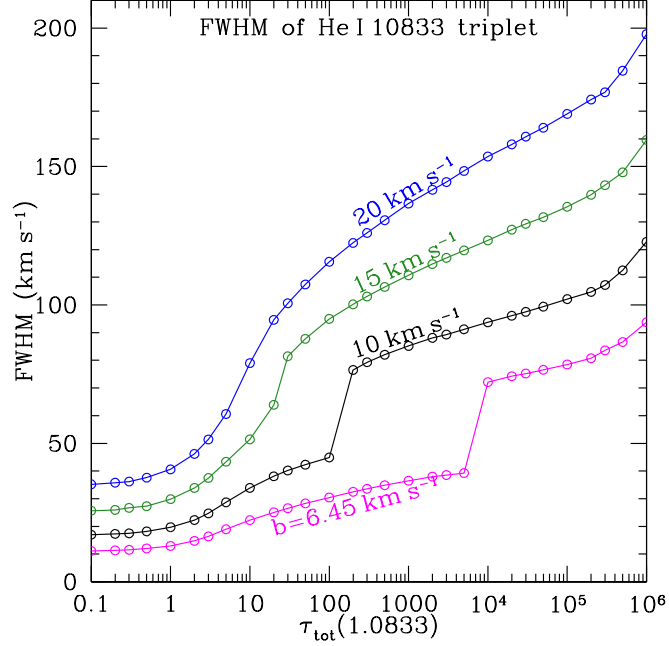


**Figure 9.** Full width at half maximum (FWHM) of the line profile (in velocity units), as a function of the optical depth parameter  $\tau_{\text{tot}}$ , for four values of the Doppler broadening parameter  $b$ .

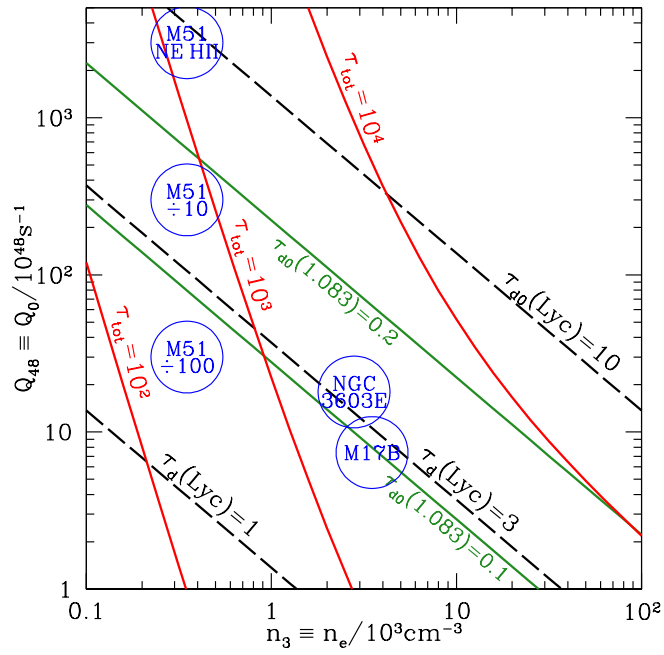


**Figure 10.** Red lines: contours of constant 1.0833 $\mu$ m scattering optical depth  $\tau_{\text{tot}}$  (for  $\xi = 1$ ) on the  $n_3 - Q_{48}$  plane. Black lines: contours of constant dust optical depth  $\tau_{d,0}$  for Lyman continuum (dashed) and 1.0833 $\mu$ m (green). Also shown are  $(n_3, Q_{48})$  for M17B, NGC 3603 Source E, and three possibilities for NE-Strip H II in M51 (see Section 6.1).

5. HE I 1.0833 $\mu$ m EMISSION FROM DUSTY H II REGIONS5.1. *Parameter Space*

Figure 10 shows (in red) contours of constant  $\tau_{\text{tot}}$  on the  $n_3 - Q_{48}$  plane, for dustless Strömgren spheres, and assuming  $\text{He}^+/\text{H}^+ = 0.10$ . The locations of M17B and NGC 3603 Source E are indicated. Three possibilities are shown for NE-Strip H II in M51. It is evident that many H II regions are expected to have  $\tau_{\text{tot}} \gtrsim 10^3$ , with strong resonant scattering of the He I 1.0833 $\mu$ m triplet.

The optical properties of dust within H II regions are uncertain. For dust absorption cross section  $\sigma_d(\text{Lyc}) \approx 1 \times 10^{-21} \text{ cm}^2$  and  $\sigma_d(1.0833\mu\text{m}) \approx 3.5 \times 10^{-23} \text{ cm}^2$  per H nucleon (B. S. Hensley & B. T. Draine 2020; K. D. Gordon et al. 2023)<sup>7</sup>, the center-to-edge absorption optical depths for the H II region are

$$\tau_{d,0}(\text{Lyc}) \approx 0.9 Q_{48}^{1/3} n_3^{1/3} \quad (19)$$

$$\tau_{d,0}(1.0833\mu\text{m}) \approx 0.033 Q_{48}^{1/3} n_3^{1/3} . \quad (20)$$

and the dust optical depth from the center to the edge of the He II zone is

$$\tau_d(1.0833\mu\text{m}) = \xi^{1/3} \tau_{d,0} . \quad (21)$$

Figure 10 also shows contours of constant  $\tau_d(\text{Lyc})$  (in black) and  $\tau_{d,0}(1.0833\mu\text{m})$  (in green) on the  $n_3 - Q_{48}$  plane. For example: an H II region with  $Q_{48} = 10^2$ ,  $n_3 = 1$ ,  $\xi = 1$ , and  $b = 10 \text{ km s}^{-1}$  would have  $\tau_{\text{tot}} \approx 1800$  (from Equation 12), and center-to-edge  $\tau_d(1.0833\mu\text{m}) \approx 0.16$  (from Equation 20).

For center-to-edge optical depth  $\tau_d$  for dust absorption, nonresonant lines (such as H I Pa $\gamma$ ) are suppressed by a factor  $f_{\text{esc}}(\tau_{d,0})$ , where

$$f_{\text{esc}}(x) \equiv \frac{3}{8x^3} [2x^2 - 1 + (1 + 2x)e^{-2x}] \quad (22)$$

$$= 1 - \frac{3}{4}x + \frac{2}{5}x^2 - \frac{1}{6}x^3 \dots \quad \text{for } x \ll 1 \quad (23)$$

is the exact result for the photon escape fraction from a sphere with uniform emission per volume and uniform absorption with center-to-edge optical depth  $x$ .

With resonant trapping enhancing the path length traveled, the escape probability for He I 1.0833 $\mu$ m triplet photons is reduced. A simple estimate for the escape probability is

$$p_{\text{esc}} \approx f_{\text{esc}} \left( \tau_d \times \frac{\langle L_{\text{path}} \rangle}{R} \right) , \quad (24)$$

where  $\langle L_{\text{path}} \rangle/R$  is given by Eq. (17) (based on calculations for the dustless case).

As a test, Figure 11 shows the results of accurate Monte-Carlo calculations for  $\tau_{\text{tot}} = 1800$ ,  $b = 10 \text{ km s}^{-1}$ , for both  $\tau_d = 0$  (blue curve) and  $\tau_d = 0.16$  (red curve). For this case, Equation (17) predicts  $\langle L_{\text{path}} \rangle/R \approx 5.70$ , and Equation (24) gives  $p_{\text{esc}} \approx f_{\text{esc}}(0.911) = 0.554$ , in good agreement with  $p_{\text{esc}} = 0.527$  from the Monte-Carlo calculation, confirming that Equation (24) provides a reasonable estimate for  $p_{\text{esc}}$  if direct Monte-Carlo calculations are unavailable. The spectrum for  $\tau_d = 0$ , scaled down by the estimate  $f_{\text{esc}} = 0.554$  (broken curve), is in fair agreement with the actual spectrum for  $\tau_d = 0.16$  (red curve). This indicates that the suite of spectra calculated for dustless H II regions can be used (with Equations 24 and 17) to estimate He I 1.0833 $\mu$ m for dusty H II regions for  $\tau_d \lesssim 0.2$ .

<sup>7</sup> We take the absorption cross section  $\sigma_d = 3.5 \times 10^{-23} \text{ cm}^2/\text{H}$  from the Astrodust model (B. S. Hensley & B. T. Draine 2023).

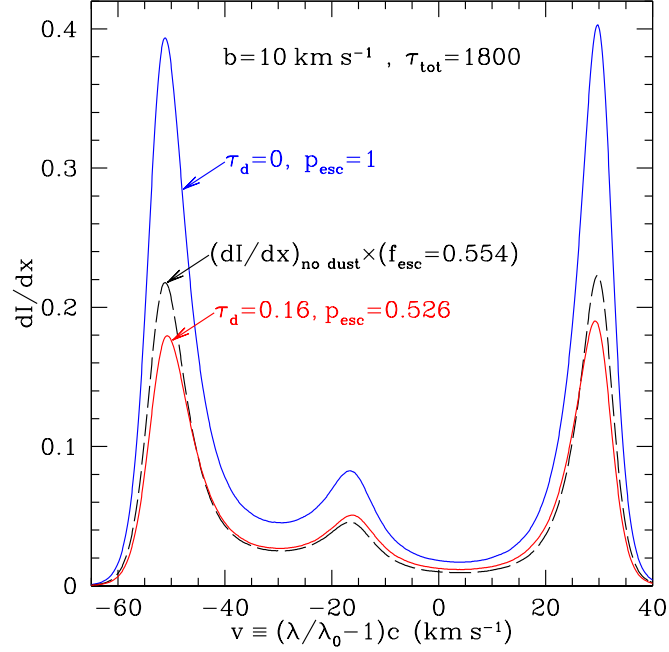


**Figure 11.** For  $b = 10 \text{ km s}^{-1}$  and  $\tau_{\text{tot}} = 1800$ : Spectrum of the escaping photons in the absence of dust (blue), and for dust with center-to-edge absorption optical depth  $\tau_d(1.0833\mu\text{m}) = 0.16$  (red curve). The black broken curve is the dustless spectrum multiplied by  $f_{\text{esc}}(\tau_d \times \langle L \rangle / R)$ , with  $\langle L \rangle / R$  obtained from Equation (17). For this case, the approximation slightly overestimates the line power by  $\sim 5\%$ :  $f_{\text{esc}} = 0.554 > p_{\text{esc}} = 0.526$ ). The shape of the spectrum with dust is similar to the attenuated dustless spectrum, but differs in detail: lower at the red-shifted and blue-shifted peaks, but slightly higher at the central peak).

For  $Q_{48}n_3 \gtrsim 10$  (i.e.,  $\tau_{d,0}(\text{Lyc}) \gtrsim 2$ ), absorption of ionizing radiation by dust becomes significant, and radiation pressure on dust and gas causes the H II to develop a shell-like structure (B. T. Draine 2011b). For  $Q_{48}n_3 \gtrsim 10$ , accurate calculations of the emission spectrum should allow for the nonuniform density of both dust and gas. However, in the absence of such calculations, a reasonable approximation is to use Equations (24) and (17) to estimate the effects of dust, with  $Q_{48}$  in Equation (12) denoting the actual H photoionization rate.

Real H II regions with  $Q_{48} \gtrsim 10^2$  will be powered by many O stars, and the distribution of both the ionizing stars and the gas may be complex. In addition, there may be velocity gradients arising from gas flows. It will not be surprising if actual spectra deviate from the static, spherically-symmetric models considered here.

## 5.2. The He I 1.0833 $\mu$ m/H I Pa $\gamma$ Line Ratio

The He I 1.0833 $\mu$ m/H I Pa $\gamma$  1.09441 $\mu$ m line ratio is useful for measuring the  $\text{He}^+/\text{H}^+$  ratio, because the nearly identical wavelengths imply that differential extinction due to foreground dust will not affect the line ratio. However, the line ratio will be affected by radiative trapping of the He I 1.0833 $\mu$ m photons within the H II region.

He I 1.0833 $\mu$ m is both emitted and resonantly trapped only in the region where He is ionized; if  $\xi < 1$ , this will be only the central part of the H II region. The He I 1.0833 $\mu$ m/H I Pa $\gamma$  ratio for

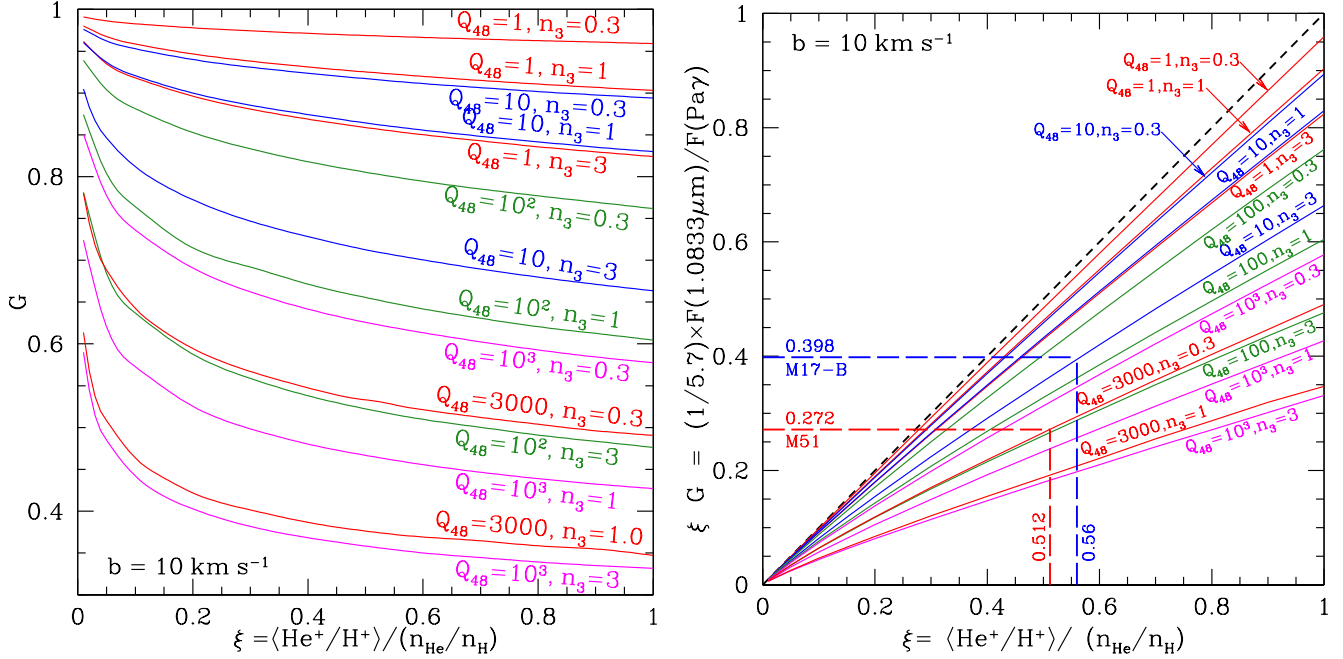


**Figure 12.** (a) function  $G(\xi)$  showing extra attenuation of  $1.0833\mu\text{m}$  relative to  $\text{Pa}\gamma$  due to resonant trapping, for selected values of  $Q_{48}$  and  $n_3$  (see text). (b)  $\xi G$  as a function of  $\xi$ . Dashed lines show how  $\xi$  (the actual  $\text{He}^+/\text{H}^+$  ratio) can be determined from the observed  $F(1.0833\mu\text{m})/F(\text{Pa}\gamma)$  flux ratios for M17-B and M51 NE-Strip H II.

radiation emerging from the H II region can be estimated to be

$$\frac{F(1.0833\mu\text{m})}{F(\text{Pa}\gamma)} \approx \left[ \frac{j(1.0833\mu\text{m})}{j(\text{Pa}\gamma)} \frac{\langle n(\text{He}^+) \rangle}{\langle n(\text{H}^+) \rangle} \right] \times G(\tau_{\text{tot}}, \xi, \tau_{\text{d},0}) \quad (25)$$

$$G(\tau_{\text{tot}}, \xi, \tau_{\text{d},0}) = \frac{p_{\text{esc}}(\tau_{\text{tot}}, \xi^{1/3} \tau_{\text{d},0}) \exp[-(1 - \xi^{1/3}) \tau_{\text{d},0}]}{f_{\text{esc}}(\tau_{\text{d},0})} \quad (26)$$

where  $\langle n(\text{He}^+) \rangle$  and  $\langle n(\text{H}^+) \rangle$  are electron-density-weighted averages, and  $f_{\text{esc}}(\tau)$  is given by Equation (22). The quantity in square brackets in (25) is the intrinsic  $F(1.0833\mu\text{m})/F(\text{Pa}\gamma)$  ratio;  $G$  is the suppression due to resonant trapping. The factor  $\exp[-(1 - \xi^{1/3}) \tau_{\text{d},0}]$  in Equation (26) is an estimate for the attenuation of the  $1.0833\mu\text{m}$  photons as they traverse the outer zone of the H II region where He is neutral.

The function  $G(\xi)$  is shown in Figure 12a, for selected values of  $(Q_{48}, n_3)$ . For large values of  $Q_{48}$  and  $n_3$  (and  $\xi \gtrsim 0.1$ )  $G$  can be significantly smaller than 1: the observed flux ratio is significantly smaller than the intrinsic flux ratio.

An H II region has  $\langle \text{He}^+/\text{H}^+ \rangle = (\text{n}_{\text{He}}/\text{n}_{\text{H}}) \xi$ . For case B recombination at  $T_e = 9000\text{ K}$  and  $n_e \approx 10^3 \text{ cm}^{-3}$  we have  $4\pi j(1.0833\mu\text{m}) = 7.065 \times 10^{-25} \text{ erg cm}^3 \text{ s}^{-3}$  (G. Del Zanna & P. J. Storey 2022) and  $4\pi j(\text{Pa}\gamma) = 1.245 \times 10^{-26} \text{ erg cm}^3 \text{ s}^{-1}$  (P. J. Storey & D. G. Hummer 1995). Thus, for He abundance  $\text{n}_{\text{He}}/\text{n}_{\text{H}} = 0.10$  we expect

$$\frac{1}{5.7} \frac{F(1.0833\mu\text{m})}{F(\text{Pa}\gamma)} \approx \xi G(\tau_{\text{tot}}, \xi, \tau_{\text{d},0}) \quad . \quad (27)$$

Figure 12b shows  $\xi G = [F(1.0833\mu\text{m})/F(\text{Pa}\gamma)]/5.7$  as a function of  $\xi$ , the fraction of the He in the H II region that is ionized, for selected values of  $(Q_{48}, n_3)$ .

Figure 12b can be used to determine the actual value of  $\text{He}^+/\text{H}^+$  from the observed ratio  $F(1.0833\mu\text{m})/F(\text{Pa}\gamma)$ : the horizontal red dashed line in Figure 12b is the observed value of  $(1/5.7)(F(1.0833\mu\text{m})/F(\text{Pa}\gamma)) = 0.272$  for NE-Strip H II in the galaxy M51 (B. T. Draine et al. 2025). If it is assumed that there is no differential extinction between 1.0833 $\mu\text{m}$  and  $\text{Pa}\gamma$  1.0941 $\mu\text{m}$ , we would estimate  $\xi = (\text{He}^+/\text{H}^+)/(n_{\text{He}}/n_{\text{H}}) \approx 0.27$ . However, NE-Strip H II appears to be characterized by  $Q_{48} = 3000$ ,  $n_3 = 0.3$ ; for this case we see that the observed flux ratio corresponds to  $\xi \approx 0.51$ , and  $\text{He}^+/\text{H}^+ \approx (n_{\text{He}}/n_{\text{H}})\xi \approx 0.051$  – correcting for the effects of radiative trapping raises the estimate for  $\text{He}^+/\text{H}^+$  from  $\sim 0.027$  to  $\sim 0.051$ .

Similarly, the dashed blue line in Figure 12b is for the observed fluxes from M17-B (see Section 6.2). For this case ( $Q_{48} \approx 10$ ,  $n_3 \approx 3$ ) we estimate  $\xi \approx 0.56$  – correcting for the effects of radiative trapping raises the estimate for  $\text{He}^+/\text{H}^+$  from  $\sim 0.040$  to  $\sim 0.056$ .

## 6. DISCUSSION

The importance of resonant scattering of H I Ly $\alpha$  in H II regions has long been recognized, but the effects cannot be directly observed because Ly $\alpha$  photons escaping from the H II region are strongly scattered by H I outside the H II region, and absorbed by interstellar dust. Thus, it has not been possible to test predictions for the spectrum of Ly $\alpha$  photons emerging from H II regions.

The He I 1.0833 $\mu\text{m}$  triplet, however, does allow us to test our theory of resonant scattering. For bright H II regions ionized by early-type O stars, He I 1.0833 $\mu\text{m}$  emission can be strong, and the population of metastable  $\text{He}^0 2^3\text{S}_1$  is large enough for the optical depth  $\tau_{\text{tot}}$  for resonant scattering of He I 1.0833 $\mu\text{m}$  photons within the H II region to be large. Because the population of metastable  $\text{He}^0 2^3\text{S}_1$  is negligible outside the H II region (N. Indriolo et al. 2009), the He I 1.0833 $\mu\text{m}$  photons will travel unimpeded (except by dust) after escaping the H II region, allowing remote observations to test theoretical predictions for the spectrum.

The observable effects of resonant scattering of He I 1.0833 $\mu\text{m}$  will be most conspicuous in high surface brightness H II regions with large  $\text{EM}_R$ . We consider three illustrative examples.

### 6.1. Example: Giant H II Regions in M51

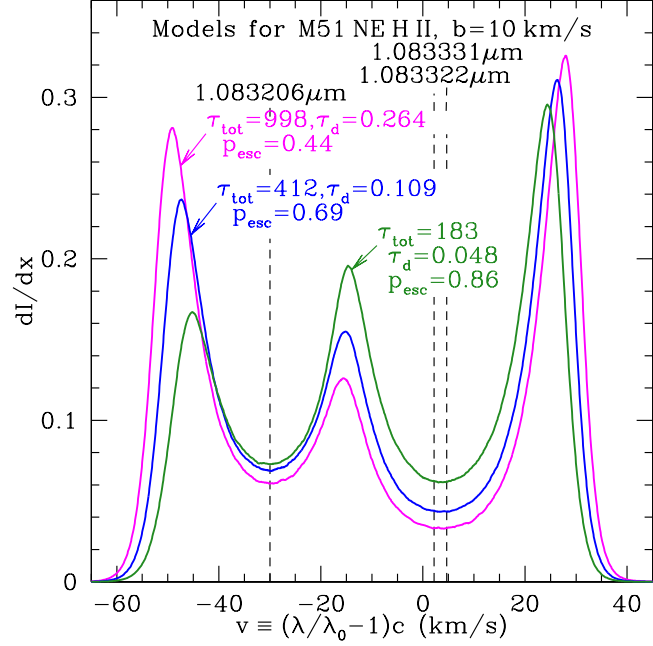
The star-forming region “NE-Strip H II” in M51 is estimated to be powered by stars with  $Q_{48} \approx 3 \times 10^3$  (B. T. Draine et al. 2025). K. V. Croxall et al. (2015) estimated  $n_e \approx 300 \pm 50 \text{ cm}^{-3}$  for this region (“NGC5194+91.0+69.0”). However, we don’t know if the observed emission is dominated by a single giant H II region, or is due to many smaller ones. We consider three possibilities:

1. A single giant H II region with  $Q_{48} = 3000$ ,  $\tau_{\text{tot}} \approx 10^3$ , and  $\xi = 0.57$ .
2. Ten giant H II regions, each with  $Q_{48} = 300$ ,  $\tau_{\text{tot}} \approx 410$ , and  $\xi = 0.40$ .
3. 100 smaller H II regions, each with  $Q_{48} = 30$ ,  $\tau_{\text{tot}} \approx 180$ , and  $\xi = 0.34$ .

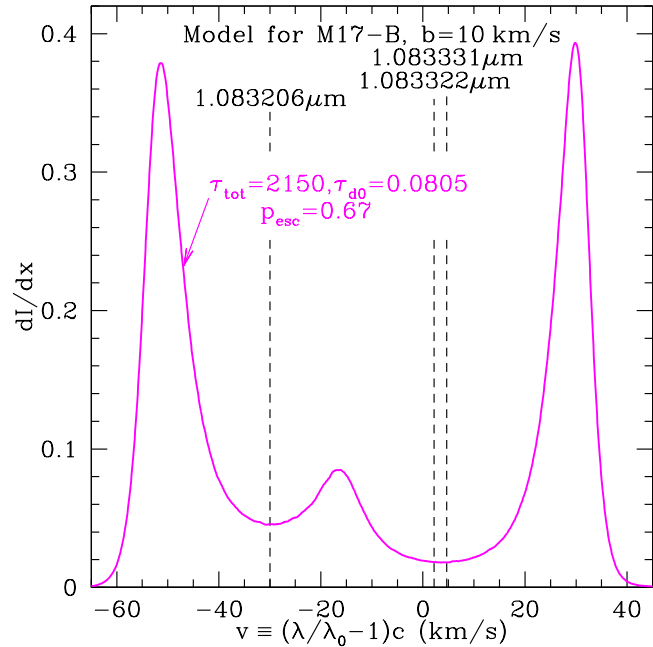
For all three cases we assume  $n_3 \approx 0.3$ , and  $b \approx 10 \text{ km s}^{-1}$ .

Figure 13 shows calculated spectra for the three cases. As the number of individual H II regions increases, the central peak increases, and the blue peak decreases. All cases shown are consistent with the observed  $F(1.0833\mu\text{m})/F(\text{Pa}\gamma) \approx 1.7$ , but  $\text{He}^+/\text{H}^+$  varies from 0.057 to 0.034. If  $\xi \approx 0.57$ , the stellar population should have  $Q_1/Q_0 \approx 0.088$ , corresponding to spectral type intermediate between O8.5V and O9V (F. Martins et al. 2005).

1 – 1.2 $\mu\text{m}$  spectroscopy of this region with the Keck NIRSPEC spectrograph ( $R = 25000$ ; I. S. McLean et al. 1998) or the Calar Alto 3.5m CARMENES spectrograph ( $R = 80000$ ; A. Quirrenbach et al. 2014) would be able to test the predictions in Figure 13, and distinguish between the predictions for one giant H II region, versus many smaller regions. The differing estimates of  $\text{He}^+/\text{H}^+$  could be directly tested using radio recombination lines.



**Figure 13.** Models for He I  $1.0833\mu\text{m}$  emission from NE-Strip H II in M51 coming from 1, 10, or 100 H II regions (see text). The model with 1 giant H II region (magenta,  $\tau_{\text{tot}} = 998$ ) has  $\text{He}^+/\text{H}^+ \approx 0.057$ , the model with 10 giant H II regions (blue,  $\tau_{\text{tot}} = 412$ ) has  $\text{He}^+/\text{H}^+ \approx 0.040$ , and the model with 100 H II regions (green,  $\tau_{\text{tot}} = 183$ ) has  $\text{He}^+/\text{H}^+ \approx 0.035$ . Spectra of escaping photons are normalized to  $\int (dI/dx)dx = 1$ .



**Figure 14.** Predicted line profile for M17-B (see text) for  $b = 10 \text{ km s}^{-1}$ , and  $\tau_{\text{tot}} = 2000$  (see text). Two strong peaks are expected, at  $v \approx -52 \text{ km s}^{-1}$  and  $+30 \text{ km s}^{-1}$ , and a weaker central peak at  $v \approx -16 \text{ km s}^{-1}$ .

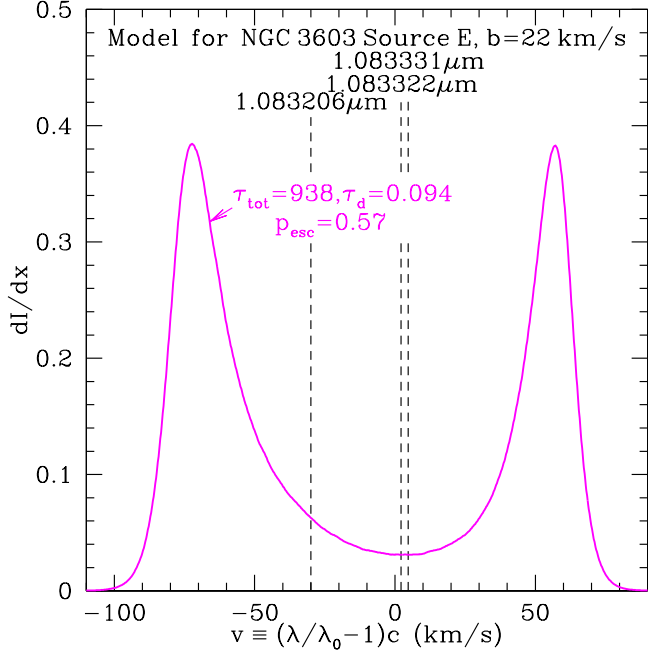


**Figure 15.** Predicted line profile for NGC 3603 Source E for  $b = 22 \text{ km s}^{-1}$ , and  $\tau_{\text{tot}} = 1300$ , with dust absorption (see text). Two strong peaks are expected, at  $v \approx -80 \text{ km s}^{-1}$  and  $+60 \text{ km s}^{-1}$ .

### 6.2. Example: M17-B

C. Boersma et al. (2023) obtained JWST NIRSpec and MIRI-MRS spectra of position M17-B in the M17 H II region. M17-B coincides with the radio continuum peak (H. E. Matthews et al. 1979; K. Akabane et al. 1989), with  $\text{EM} \equiv \int n_e n(\text{H}^+) ds = 1.7 \times 10^{25} \text{ cm}^{-5}$  and  $n_e \approx 3500 \text{ cm}^{-3}$  (H. E. Matthews et al. 1979). We note the consistency between  $\text{EM} \approx 1.7 \times 10^{25} \text{ cm}^{-5}$  from the radio observations and  $\text{EM} \approx 1.2 \times 10^{25} \text{ cm}^{-5}$  from modeling the recombination lines observed by NIRSpec and MIRI-MRS through dust with  $A_V \approx 10.5$  mag (B. T. Draine et al. 2025).

Here we suppose that the M17-B peak corresponds to an H II region with  $Q_{48} = 7.4$  (10% of the estimated ionization rate for the entirety of M17; B. A. Binder & M. S. Povich 2018). With  $n_e \approx 3500 \text{ cm}^{-3}$ , this would have peak  $\text{EM} = 2 \text{EM}_R = 2 \times 10^{25} \text{ cm}^{-5}$ , consistent with the radio determination.

The observed spectrum (C. Boersma et al. 2023) has  $F(1.0833\mu\text{m})/F(\text{Pa}\gamma) = 2.27$ ; the inferred He ionization (see Figure 12b) is

$$\frac{\text{He}^+}{\text{H}^+} = 0.10 \xi \approx \frac{F(1.0833\mu\text{m})/F(\text{Pa}\gamma)}{57 G} = 0.056 \quad (28)$$

47% larger than the value 0.038 obtained without allowing for the effects of resonant trapping (B. T. Draine et al. 2025).

Figure 14 shows a Monte-Carlo calculated spectrum with radiative trapping and extinction by dust included, for  $b = 10 \text{ km s}^{-1}$ . Spectroscopy of the He I  $1.0833\mu\text{m}$  profile in M17-B with CARMENES, NIRSPEC, or the VLT X-shooter ( $R = 11300$ ; J. Vernet et al. 2011) can test whether the He I  $1.0833\mu\text{m}$  emission from M17-B agrees with the predicted spectra in Figure 14.

### 6.3. Example: NGC 3603

The giant H II region NGC 3603 has a number of locations with very high EM. Radio continuum observations of Source E with  $7''$  resolution find  $\text{EM} \approx 1.4 \times 10^{25} \text{ cm}^{-5}$  (C. G. De Pree et al. 1999); we estimate the center-to-edge  $\text{EM}_R \approx 1.0 \times 10^{25} \text{ cm}^{-5}$  for Source E.

The observed radio recombination lines imply electron temperature  $T_e \lesssim 9000$  K (C. G. De Pree et al. 1999). The He90 $\alpha$  line profile is consistent with  $b \approx 22$  km s $^{-1}$ , requiring that the line width be dominated by a combination of turbulence and fluid flow, possibly expansion. The present calculations do not include systematic flow: we assume that the observed  $b = 22$  km s $^{-1}$  is due to a combination of thermal broadening and microturbulence.

The He90 $\alpha$ /H90 $\alpha$  line ratio is consistent with the He being fully ionized (He $^+$ /H $^+ \approx 0.10$ ), so we take  $\xi \approx 1$ . From Equation (12) we estimate  $\tau_{\text{tot}} \approx 940$ . Figure 15 shows the predicted line profile for  $b = 22$  km s $^{-1}$  and  $\tau_{\text{tot}} = 940$  including dust. The predicted spectrum has FWHM  $> 150$  km s $^{-1}$ . We predict that the He I 1.0833 $\mu\text{m}$  emission will appear as two strong peaks, at  $v \approx -80$  km s $^{-1}$  and  $+60$  km s $^{-1}$ .

Spectral resolution  $R \equiv \lambda/\Delta\lambda \gtrsim 2 \times 10^4$  would be required to measure the predicted  $\sim 20$  km s $^{-1}$  widths of each of the two predicted peaks, which would be possible with instruments such as the WINERED spectrograph (S. Otsubo et al. 2016) on Magellan. However,  $R = 11300$  ( $\Delta v = 27$  km s $^{-1}$ ) spectroscopy with the VLT X-shooter (J. Vernet et al. 2011) would be sufficient to measure the predicted  $\sim 140$  km s $^{-1}$  splitting of the two peaks in the profile, and confirm the deep central minimum predicted in Figure 15.

#### 6.4. Other Processes Affecting He I 1.0833 $\mu\text{m}$ Emission

Above we have been assuming that He I 1.0833 $\mu\text{m}$  photons are injected as a result of standard “case B” recombination of He $^+$  with thermal electrons. However, the rate of injection of 1.0833 $\mu\text{m}$  photons can be larger due to two processes:

1. He atoms that are in the  $2^3\text{S}_1$  metastable level can undergo inelastic electron collisions that excite the  $2^3\text{P}_J^o$  level, followed by emission of an additional 1.0833 $\mu\text{m}$  photon. The fractional increase in 1.0833 $\mu\text{m}$  emission due to collisional excitation of  $2^3\text{P}_J^o$  is

$$\frac{n_e k_e}{A_{\text{ms}} + n_e k_d} , \quad (29)$$

where  $k_e$  is the rate coefficient for  $2^3\text{S}_1 \rightarrow 2^3\text{P}$  and  $k_d \approx 3.3 \times 10^{-8}$  cm $^3$  s $^{-1}$  is the rate coefficient for collisional transitions from  $2^3\text{S}_1$  to singlet states. However,  $k_e/k_d \lesssim 0.014$  for  $T \lesssim 10^4$  K (using rates from I. Bray et al. 2000) so this process can be neglected.

2. When  $N(2^3\text{S}_1)$  is large, radiative trapping can “convert” 3889.7 Å photons into 4.296 $\mu\text{m}$ , 7067.1 Å, and 1.0833 $\mu\text{m}$  photons (see Figure 1), as originally pointed out by S. R. Pottasch (1962). However, this can increase the emission of 1.0833 $\mu\text{m}$  photons by at most 21% for  $\tau_{\text{tot}} \gtrsim 10^3$ , so this is not a major correction.

#### 6.5. He I Line Ratios

Resonant trapping of He I 1.0833 $\mu\text{m}$  and other permitted transitions to  $2^3\text{S}_1$  (e.g.,  $2^3\text{S}_1 - 3^3\text{P}^o$  3890 Å and  $2^3\text{S}_1 - 4^3\text{P}^o$  3189 Å) can suppress the power in these lines, and enhance the emission in other lines (e.g.,  $3^3\text{S}_1 - 2^3\text{P}^o$  7067 Å), as originally pointed out by S. R. Pottasch (1962).

A number of authors have estimated the effects of radiative transfer on observed line He I line ratios (e.g., R. R. Robbins 1968b; D. E. Osterbrock 1989; R. A. Benjamin et al. 2002; K. P. M. Blagrave et al. 2007), using different estimates for the “escape probability”  $\beta$  for He I 1.0833 $\mu\text{m}$  photons. The present Monte-Carlo study provides improved estimates for  $\beta$  from a spherical nebula, with values of  $\beta$  that can be significantly below previous estimates (see Figure 4). A future paper will use the escape probabilities obtained here to recalculate the effects of resonant scattering on He I line ratios.

## 7. SUMMARY

1. Monte-Carlo radiative transfer calculations have been carried out for resonant scattering by metastable He $^0$   $2^3\text{S}_1$  in dustless H II regions, using exact partial redistribution and Voigt line

profiles. The mean number of scatterings  $\langle N_{\text{sca}} \rangle$  and the mean pathlength  $\langle L_{\text{path}} \rangle$  traveled for He I 1.0833 $\mu$ m triplet photons were determined as functions of He I 1.0833 $\mu$ m optical depth  $\tau_{\text{tot}}$ , for different values of  $b$ . Simple fitting formulae for  $\langle N_{\text{sca}} \rangle$  and  $\langle L_{\text{path}} \rangle$  are given.

2. Resonant scattering by metastable He<sup>0</sup> 2<sup>3</sup>S<sub>1</sub> can produce unusual multi-peaked line profiles for the He I 1.0833 $\mu$ m triplet emission from H II regions.
3. For normal H II region conditions ( $b \approx 10 \text{ km s}^{-1}$ ,  $10^2 \lesssim \tau_{\text{tot}} \lesssim 10^3$ ), the overall He I 1.0833 $\mu$ m emission can be blue-shifted by up to  $\sim 14 \text{ km s}^{-1}$ .
4. For H II regions with  $Q_{48}n_3 \gtrsim 10$ , dust can significantly reduce the emission in He I 1.0833 $\mu$ m, and influence the shape of the emission profile. Estimates of He<sup>+</sup>/H<sup>+</sup> using He I 1.0833 $\mu$ m/H I Pa $\gamma$  should allow for the resonant-scattering-enhanced attenuation of He I 1.0833 $\mu$ m by dust. Monte-Carlo calculations have been carried out to explore the effects of dust, for dust abundances appropriate to star-forming galaxies with near-solar metallicities.
5. For Milky Way dust abundances, we estimate the effects of resonant trapping on the He 1.0833 $\mu$ m/H Pa $\gamma$  1.0941 $\mu$ m line ratio. If  $Q_{48}$  and  $n_3$  can be estimated, Figure 12b can be used to estimate He<sup>+</sup>/H<sup>+</sup>.
6. In low metallicity systems, dust attenuation will be less important, but resonant trapping will continue to produce the unusual multipeaked line profiles found here.
7. We predict He I 1.0833 $\mu$ m line profiles for the Galactic H II regions M17-B and NGC 3603, and for the star-forming region “NE-Strip H II” in the Whirlpool galaxy M51. The profiles typically consist of two strong peaks, separated by  $\sim 75$ – $140 \text{ km s}^{-1}$ , with the centroid of the He I 1.0833 $\mu$ m emission blue-shifted by  $\sim 13 \text{ km s}^{-1}$  relative to other lines. For modest  $\tau_{\text{tot}}$  a central peak at  $-18 \text{ km s}^{-1}$  is also present. The relative strength of the central peak decreases as  $\tau_{\text{tot}}$  is increased. The splitting, blue shift, and central peak could be confirmed with  $R \gtrsim 10^4$  spectroscopy.

## ACKNOWLEDGEMENTS

I am grateful to Kwang-il Seon for very helpful communications regarding Ly $\alpha$  scattering, and to the anonymous referee for comments that led to improvement of the manuscript. I thank Giulio Del Zanna, Jim Gunn, and Dina Gutkowicz-Krusin for helpful discussions, and Robert Lupton for continued availability of the SM plotting package.

## APPENDIX

### A. MONTE-CARLO RADIATIVE TRANSFER

#### A.1. *Opacity*

Consider scatterers with lower level  $E_\ell$  (e.g., the metastable 1s2s 3S<sub>1</sub> state) and  $N$  excited states,  $E_u$ ,  $u = 1 - N$ , with degeneracies  $g_u$ , Einstein  $A$  coefficients  $A_{u\ell}$ , and slightly different wavelengths  $\lambda_{u\ell}$ . It is convenient to measure the photon frequency by the dimensionless Doppler shift  $x_j$  relative to the multiplet centroid  $\lambda_c$ ,

$$x = \frac{\lambda_c/\lambda - 1}{b/c} \quad . \quad (\text{A1})$$

The dimensionless Doppler shift of the photon relative to the local  $\lambda_{u\ell}$  line is  $x + \Delta_u$  where

$$\Delta_u \equiv \left( \frac{\lambda_{u\ell}}{\lambda_c} - 1 \right) \frac{c}{b} \quad . \quad (\text{A2})$$

The attenuation coefficient

$$\alpha(x) = n_{\text{H}} \sigma_{\text{d}} + n(\text{He } 2^3\text{S}_1) \sum_{u=0}^2 \sigma_{\ell u}(x) \quad (\text{A3})$$

$$\sigma_{\ell u}(x) = \frac{g_u A_{u\ell} \lambda_{u\ell}^3}{8\pi^2 b} \phi(x + \Delta_u, a) \quad , \quad (\text{A4})$$

where  $\sigma_{\text{d}}$  is the dust absorption cross section per H nucleon. The Voigt line profile  $\phi(x, a)$  is obtained by table look-up from tables generated using approximations from [B. Armstrong \(1967\)](#).

### A.2. Injection

Photons are injected uniformly throughout the spherical volume, with initial frequencies  $x$  drawn from the Voigt line profile  $\phi(x)$ , and random directions of propagation  $\hat{\mathbf{n}}$ . All results for regions with dust were calculated using at least  $10^6$  (in most cases  $10^7$ ) injected photons to ensure statistical accuracy.

### A.3. Transport

Let  $s$  measure path length in line-center optical depth units:

$$ds = \tau_{\text{tot}} \frac{dL}{R} \quad , \quad (\text{A5})$$

where  $L$  is physical path length. Let  $t = (r/R)\tau_{\text{tot}}$  be the line-center optical depth from the center of the sphere to a location at radius  $r$ . Let  $\tau_{\text{d}} = n_{\text{H}} \sigma_{\text{d}} R$  be the dust absorption optical depth from center to edge.

Let  $t_j$  be the location of a photon with Doppler shift  $x_j$ , traveling in direction  $\hat{\mathbf{n}}_j$ . Define the direction cosine

$$\mu_j \equiv \hat{\mathbf{n}}_j \cdot \hat{\mathbf{r}}_j \quad , \quad (\text{A6})$$

where  $\hat{\mathbf{r}}_j$  is the radial direction at the photon's location. To escape, the photon must traverse a path length

$$s_{\text{esc}} = \left\{ \left[ \tau_{\text{tot}}^2 - t_j^2 (1 - \mu_j^2) \right]^{1/2} - t_j \mu_j \right\} \quad . \quad (\text{A7})$$

The probability of escape for this photon is

$$P_{\text{esc}} = \exp[-\tau(s_{\text{esc}})] \quad (\text{A8})$$

$$\tau(s) = \int_0^s \alpha(x_j, s') \frac{R}{\tau_{\text{tot}}} ds' \quad . \quad (\text{A9})$$

The probability of scattering or absorption in an interval  $[s, s + ds]$  is

$$dP = \exp[-\tau(s)] d\tau \quad . \quad (\text{A10})$$

A random number  $\mathcal{P}_1$  is drawn<sup>8</sup> from a distribution uniform on  $[0, 1]$ . The photon escapes if  $\mathcal{P}_1 > 1 - P_{\text{esc}}$ ; if  $\mathcal{P}_1 < 1 - P_{\text{esc}}$  there is an event (either scattering or absorption) after traversing optical depth

$$\tau_j = -\ln(1 - \mathcal{P}_1) \quad . \quad (\text{A11})$$

<sup>8</sup> We employ the Mersenne Twister random number generator ([M. Matsumoto & T. Nishimura 1998](#)), translated into Fortran by Tsuyoshi Tada.

If we take  $\alpha(x_j)$  to be constant along the path, then

$$s_j = \frac{-\ln(1 - \mathcal{P}_1)}{\alpha(x_j)} . \quad (\text{A12})$$

After traveling a pathlength  $s_j$ , the event (scattering or absorption) will be at

$$t_{j+1} = [t_j^2 + 2\mu_j t_j s_j + s_j^2]^{1/2} , \quad (\text{A13})$$

with new direction cosine  $\tilde{\mu}_{j+1} \equiv \hat{\mathbf{n}}_j \cdot \hat{\mathbf{r}}_{j+1}$ :

$$\tilde{\mu}_{j+1} = \left[ 1 - \left( \frac{t_j}{t_{j+1}} \right)^2 (1 - \mu_j^2) \right]^{1/2} \quad \text{if } s > -\mu_j t_j \quad (\text{A14})$$

$$= - \left[ 1 - \left( \frac{t_j}{t_{j+1}} \right)^2 (1 - \mu_j^2) \right]^{1/2} \quad \text{if } s < -\mu_j t_j \quad (\text{A15})$$

*prior* to scattering (or absorption).

The probability that the event is resonant scattering by transition  $\ell \rightarrow u$  is

$$P_{\ell u} = \frac{n_\ell \sigma_{\ell u}(x_j)}{\alpha(x_j)} . \quad (\text{A16})$$

A random number  $\mathcal{P}_2 \in [0, 1]$  is drawn to determine whether the event is resonant scattering by transition  $\ell \rightarrow u$ . If  $\mathcal{P}_2 > \sum_{u=0}^2 P_{\ell u}$ , the photon is absorbed by dust.

#### A.4. Direction After Scattering

Suppose that scattering takes place at  $t_{j+1}$ , with scattering angle  $\gamma_{j+1}$ . The new direction of propagation  $\hat{\mathbf{n}}_{j+1}$  will have direction cosine

$$\mu_{j+1} \equiv \hat{\mathbf{n}}_{j+1} \cdot \hat{\mathbf{r}}_{j+1} = \tilde{\mu}_{j+1} \cos \gamma_{j+1} + (1 - \tilde{\mu}_{j+1}^2)^{1/2} \sin \gamma_{j+1} \cos \phi_{j+1} \quad (\text{A17})$$

and new dimensionless Doppler shift  $x_{j+1}$ . For unpolarized light,  $\phi_{j+1}$  is uniformly distributed in  $[0, 2\pi]$ :

$$\frac{dP_\phi}{d\phi_{j+1}} = \frac{1}{2\pi} , \quad \phi_{j+1} \in [0, 2\pi] . \quad (\text{A18})$$

and  $\cos \gamma_{j+1}$  has probability distribution

$$\frac{dP}{d\cos \gamma} = \frac{3}{8} (1 + \cos^2 \gamma) , \quad \cos \gamma \in [-1, 1] . \quad (\text{A19})$$

Equation (A19) applies for both resonant scattering (e.g., by He I 2<sup>3</sup>S<sub>1</sub>) and Thomson scattering by free electrons. After drawing a random variable  $P_\gamma$  uniformly distributed on  $[0, 1]$ , we obtain  $\cos \gamma$  using the result found by [K.-I. Seon \(2006\)](#):

$$\cos \gamma = \left[ 2(2P_\gamma - 1) + \sqrt{4(2P_\gamma - 1)^2 + 1} \right]^{1/3} - \left[ 2(2P_\gamma - 1) + \sqrt{4(2P_\gamma - 1)^2 + 1} \right]^{-1/3} . \quad (\text{A20})$$

### A.5. Frequency After Scattering

Let  $\mathbf{w}_{j+1}$  be the velocity of the scatterer in the fluid frame, at the location  $t_{j+1}$  of the scattering. We are concerned only with components of  $\mathbf{w}_{j+1}$  in the scattering plane. Define

$$w_{\parallel,j+1} \equiv \hat{\mathbf{n}}_j \cdot \mathbf{w}_{j+1} \quad (A21)$$

$$(A22)$$

$$w_{\perp,j+1} \equiv [(\hat{\mathbf{n}}_{j+1} - \cos \gamma_{j+1} \hat{\mathbf{n}}_j) \cdot \mathbf{w}_{j+1}] / \sin \gamma_{j+1} \quad . \quad (A23)$$

Neglecting recoil, the dimensionless frequency after scattering is

$$x_{j+1} = x_j + w_{\parallel,j+1} (\cos \gamma_{j+1} - 1) + w_{\perp,j+1} \sin \gamma_{j+1} \quad . \quad (A24)$$

We use the “partial redistribution function” for a line with finite intrinsic width (D. G. Hummer 1962). The exact distribution for  $w_{\parallel}$  is difficult to invert. For given  $x_j$  and transition  $\ell \rightarrow u$ , following Z. Zheng & J. Miralda-Escudé (2002), we use the “method of rejection” (W. H. Press et al. 1992) to draw  $w_{\parallel,j+1}$  from the exact distribution

$$\frac{dP}{dw_{\parallel,j+1}} \propto \frac{e^{-w_{\parallel,j+1}^2}}{(x_j + \Delta_u - w_{\parallel,j+1})^2 + a^2} \quad . \quad (A25)$$

We employ a modification of the “comparison function”  $g(x)$  used by Z. Zheng & J. Miralda-Escudé (2002): for  $x \geq 0$ :

$$g(x) = \frac{1}{(x - w_{\parallel})^2 + a^2} \quad 0 \leq x \leq C_1 \quad (A26)$$

$$= \frac{e^{-C_1^2}}{(x - w_{\parallel})^2 + a^2} \quad C_1 < x \leq C_2 \quad (A27)$$

$$= \frac{e^{-C_2^2}}{(x - w_{\parallel})^2 + a^2} \quad C_2 < x \leq C_3 \quad (A28)$$

$$= \frac{e^{-C_3^2}}{(x - w_{\parallel})^2 + a^2} \quad C_3 < x \leq C_4 \quad (A29)$$

$$= \frac{e^{-C_4^2}}{(x - w_{\parallel})^2 + a^2} \quad C_4 < x \quad . \quad (A30)$$

For  $|x| \leq 1$  we take  $C_1 = 0.5$ ,  $C_2 = 0.8$ ,  $C_3 = 1.2$ , and  $C_4 = 2.5$ ; for  $|x| > 1$ ,  $C_1 = |x|/2$ ,  $C_2 = |x| - 0.2$ ,  $C_3 = |x| + 0.2$ , and  $C_4 = |x| + 1.5$ . This greatly increases the efficiency of the method, by reducing the number of rejections.

For given  $w_{\parallel,j+1}$ , the transverse velocity  $w_{\perp,j+1}$  is drawn from the thermal distribution; the probability distribution for  $x_{j+1}$  is gaussian:

$$x_{j+1} = x_j + (\cos \gamma_{j+1} - 1) w_{\parallel,j+1} + \frac{\sin \gamma_{j+1}}{\sqrt{2}} \mathcal{P} \quad , \quad (A31)$$

where  $\mathcal{P}$  is a Gaussian random variate with zero mean and unit variance.

## REFERENCES

Adams, W. S. 1949, ApJ, 109, 354,  
doi: [10.1086/145142](https://doi.org/10.1086/145142)

Akabane, K., Sofue, Y., Hirabayashi, H., & Inoue, M. 1989, PASJ, 41, 809,  
doi: [10.1093/pasj/41.4.809](https://doi.org/10.1093/pasj/41.4.809)

Allart, R., Bourrier, V., Lovis, C., et al. 2019, *A&A*, 623, A58, doi: [10.1051/0004-6361/201834917](https://doi.org/10.1051/0004-6361/201834917)

Aller, L. H., & Liller, W. 1959, *ApJ*, 130, 45, doi: [10.1086/146695](https://doi.org/10.1086/146695)

Armstrong, B. 1967, *JQSRT*, 7, 61, doi: [10.1016/0022-4073\(67\)90057-X](https://doi.org/10.1016/0022-4073(67)90057-X)

Benjamin, R. A., Skillman, E. D., & Smits, D. P. 2002, *ApJ*, 569, 288, doi: [10.1086/339242](https://doi.org/10.1086/339242)

Binder, B. A., & Povich, M. S. 2018, *ApJ*, 864, 136, doi: [10.3847/1538-4357/aad7b2](https://doi.org/10.3847/1538-4357/aad7b2)

Blagrave, K. P. M., Martin, P. G., Rubin, R. H., et al. 2007, *ApJ*, 655, 299, doi: [10.1086/510151](https://doi.org/10.1086/510151)

Boersma, C., Allamandola, L. J., Esposito, V. J., et al. 2023, *ApJ*, 959, 74, doi: [10.3847/1538-4357/ad022b](https://doi.org/10.3847/1538-4357/ad022b)

Bonilha, J. R. M., Ferch, R., Salpeter, E. E., Slater, G., & Noerdlinger, P. D. 1979, *ApJ*, 233, 649, doi: [10.1086/157426](https://doi.org/10.1086/157426)

Bray, I., Burgess, A., Fursa, D. V., & Tully, J. A. 2000, *A&AS*, 146, 481, doi: [10.1051/aas:2000277](https://doi.org/10.1051/aas:2000277)

Cox, D. P., & Mathews, W. G. 1969, *ApJ*, 155, 859, doi: [10.1086/149916](https://doi.org/10.1086/149916)

Croxall, K. V., Pogge, R. W., Berg, D. A., Skillman, E. D., & Moustakas, J. 2015, *ApJ*, 808, 42, doi: [10.1088/0004-637X/808/1/42](https://doi.org/10.1088/0004-637X/808/1/42)

De Pree, C. G., Nysewander, M. C., & Goss, W. M. 1999, *AJ*, 117, 2902, doi: [10.1086/300892](https://doi.org/10.1086/300892)

Del Zanna, G., & Storey, P. J. 2022, *MNRAS*, 513, 1198, doi: [10.1093/mnras/stac800](https://doi.org/10.1093/mnras/stac800)

Dijkstra, M. 2019, Saas-Fee Advanced Course, 46, 1, doi: [10.1007/978-3-662-59623-4\\_1](https://doi.org/10.1007/978-3-662-59623-4_1)

Draine, B. T. 2011a, Physics of the Interstellar and Intergalactic Medium (Princeton, NJ: Princeton Univ. Press)

Draine, B. T. 2011b, *ApJ*, 732, 100, doi: [10.1088/0004-637X/732/2/100](https://doi.org/10.1088/0004-637X/732/2/100)

Draine, B. T., Sandstrom, K., Dale, D. A., et al. 2025, *ApJL*, 984, L42, doi: [10.3847/2041-8213/adc991](https://doi.org/10.3847/2041-8213/adc991)

Field, G. B. 1959, *ApJ*, 129, 551, doi: [10.1086/146654](https://doi.org/10.1086/146654)

Galazutdinov, G. A., & Krelowski, J. 2012, *MNRAS*, 422, 3457, doi: [10.1111/j.1365-2966.2012.20856.x](https://doi.org/10.1111/j.1365-2966.2012.20856.x)

Gordon, K. D., Clayton, G. C., Decleir, M., et al. 2023, *ApJ*, 950, 86, doi: [10.3847/1538-4357/accb59](https://doi.org/10.3847/1538-4357/accb59)

Hensley, B. S., & Draine, B. T. 2020, *ApJ*, 895, 38, doi: [10.3847/1538-4357/ab8cc3](https://doi.org/10.3847/1538-4357/ab8cc3)

Hensley, B. S., & Draine, B. T. 2023, *ApJ*, 948, 55, doi: [10.3847/1538-4357/acc4c2](https://doi.org/10.3847/1538-4357/acc4c2)

Hummer, D. G. 1962, *MNRAS*, 125, 21, doi: [10.1093/mnras/125.1.21](https://doi.org/10.1093/mnras/125.1.21)

Indriolo, N., Hobbs, L. M., Hinkle, K. H., & McCall, B. J. 2009, *ApJ*, 703, 2131, doi: [10.1088/0004-637X/703/2/2131](https://doi.org/10.1088/0004-637X/703/2/2131)

Kramida, A. E., Ralchenko, Y., Reader, J., & NIST ASD Team (2024). 2024, NIST Atomic Spectra Database (version 5.12) [Online] (Gaithersburg, MD: National Institute of Standards and Technology). <http://physics.nist.gov/asd>

Kulkarni, S. R. 2025, arXiv e-prints, arXiv:2509.14499, doi: [10.48550/arXiv.2509.14499](https://doi.org/10.48550/arXiv.2509.14499)

Leighly, K. M., Dietrich, M., & Barber, S. 2011, *ApJ*, 728, 94, doi: [10.1088/0004-637X/728/2/94](https://doi.org/10.1088/0004-637X/728/2/94)

Levan, P. D., Puetter, R. C., Rudy, R. J., Smith, H. E., & Willner, S. P. 1981, *ApJ*, 251, 10, doi: [10.1086/159436](https://doi.org/10.1086/159436)

Levan, P. D., Puetter, R. C., Smith, H. E., & Rudy, R. J. 1984, *ApJ*, 284, 23, doi: [10.1086/162380](https://doi.org/10.1086/162380)

Liller, W., & Aller, L. H. 1963, Proceedings of the National Academy of Science, 49, 675, doi: [10.1073/pnas.49.5.675](https://doi.org/10.1073/pnas.49.5.675)

Mansfield, M., Bean, J. L., Oklopčić, A., et al. 2018, *ApJL*, 868, L34, doi: [10.3847/2041-8213/aaf166](https://doi.org/10.3847/2041-8213/aaf166)

Martins, F., Schaerer, D., & Hillier, D. J. 2005, *A&A*, 436, 1049, doi: [10.1051/0004-6361:20042386](https://doi.org/10.1051/0004-6361:20042386)

Matsumoto, M., & Nishimura, T. 1998, *ACM Trans. Model. Comput. Simul.*, 8, 3–30, doi: [10.1145/272991.272995](https://doi.org/10.1145/272991.272995)

Matthews, H. E., Harten, R. H., & Goss, W. M. 1979, *A&A*, 72, 224

McLean, I. S., Becklin, E. E., Bendiksen, O., et al. 1998, in Society of Photo-Optical Instrumentation Engineers (SPIE) Conference Series, Vol. 3354, Infrared Astronomical Instrumentation, ed. A. M. Fowler, 566–578, doi: [10.1117/12.317283](https://doi.org/10.1117/12.317283)

Neufeld, D. A. 1990, *ApJ*, 350, 216, doi: [10.1086/168375](https://doi.org/10.1086/168375)

Nortmann, L., Pallé, E., Salz, M., et al. 2018, *Science*, 362, 1388, doi: [10.1126/science.aat5348](https://doi.org/10.1126/science.aat5348)

O'Dell, C. R. 1963, *ApJ*, 138, 1018, doi: [10.1086/147703](https://doi.org/10.1086/147703)

Oklopčić, A., & Hirata, C. M. 2018, ApJL, 855, L11, doi: [10.3847/2041-8213/aaada9](https://doi.org/10.3847/2041-8213/aaada9)

Osterbrock, D. E. 1989, *Astrophysics of Gaseous Nebulae and Active Galactic Nuclei* (Mill Valley, CA: University Science Books)

Otsubo, S., Ikeda, Y., Kobayashi, N., et al. 2016, in Society of Photo-Optical Instrumentation Engineers (SPIE) Conference Series, Vol. 9908, Ground-based and Airborne Instrumentation for Astronomy VI, ed. C. J. Evans, L. Simard, & H. Takami, 990879, doi: [10.1117/12.2233845](https://doi.org/10.1117/12.2233845)

Pan, X., Zhou, H., Liu, W., et al. 2019, ApJ, 883, 173, doi: [10.3847/1538-4357/ab40b5](https://doi.org/10.3847/1538-4357/ab40b5)

Pietrow, A. G. M., Kuckein, C., Verma, M., et al. 2025, arXiv e-prints, arXiv:2511.14331, doi: [10.48550/arXiv.2511.14331](https://doi.org/10.48550/arXiv.2511.14331)

Porter, R. L., Ferland, G. J., & MacAdam, K. B. 2007, ApJ, 657, 327, doi: [10.1086/510880](https://doi.org/10.1086/510880)

Pottasch, S. R. 1962, ApJ, 135, 385, doi: [10.1086/147278](https://doi.org/10.1086/147278)

Press, W. H., Teukolsky, S. A., Vetterling, W. T., & Flannery, B. P. 1992, *Numerical recipes in FORTRAN. The art of scientific computing* (Cambridge, UK: Cambridge Univ. Press, 2nd ed.)

Quirrenbach, A., Amado, P. J., Caballero, J. A., et al. 2014, in Society of Photo-Optical Instrumentation Engineers (SPIE) Conference Series, Vol. 9147, *Ground-based and Airborne Instrumentation for Astronomy V*, ed. S. K. Ramsay, I. S. McLean, & H. Takami, 91471F, doi: [10.1117/12.2056453](https://doi.org/10.1117/12.2056453)

Robbins, R. R. 1968a, ApJ, 151, 497, doi: [10.1086/149452](https://doi.org/10.1086/149452)

Robbins, R. R. 1968b, ApJ, 151, 511, doi: [10.1086/149453](https://doi.org/10.1086/149453)

Seon, K.-I. 2006, PASJ, 58, 439, doi: [10.1093/pasj/58.2.439](https://doi.org/10.1093/pasj/58.2.439)

Seon, K.-i., & Kim, C.-G. 2020, ApJS, 250, 9, doi: [10.3847/1538-4365/aba2d6](https://doi.org/10.3847/1538-4365/aba2d6)

Storey, P. J., & Hummer, D. G. 1995, MNRAS, 272, 41

Unno, W. 1952, PASJ, 3, 158

Vernet, J., Dekker, H., D'Odorico, S., et al. 2011, A&A, 536, A105, doi: [10.1051/0004-6361/201117752](https://doi.org/10.1051/0004-6361/201117752)

Wang, B., de Graaff, A., Davies, R. L., et al. 2025, ApJ, 984, 121, doi: [10.3847/1538-4357/adc1ca](https://doi.org/10.3847/1538-4357/adc1ca)

Wiese, W. L., & Fuhr, J. R. 2009, Journal of Physical and Chemical Reference Data, 38, 565, doi: [10.1063/1.3077727](https://doi.org/10.1063/1.3077727)

Zheng, Z., & Miralda-Escudé, J. 2002, ApJ, 578, 33, doi: [10.1086/342400](https://doi.org/10.1086/342400)